Single-cell analysis of innate spinal cord regeneration identifies intersecting modes of neuronal repair

Vishnu Muraleedharan Saraswathy[1,2], Lili Zhou[1,2] and Mayssa H. Mokalled[1,2,3]

[1] Department of Developmental Biology
Washington University School of Medicine, St. Louis, MO, USA 63110.

[2] Center of Regenerative Medicine
Washington University School of Medicine, St. Louis, MO, USA 63110.

[3] Author for correspondence: mmokalled@wustl.edu

ABSTRACT

Adult zebrafish have an innate ability to recover from severe spinal cord injury. Here, we report a comprehensive single nuclear RNA sequencing atlas that spans 6 weeks of regeneration. We identify cooperative roles for adult neurogenesis and neuronal plasticity during spinal cord repair. Neurogenesis of glutamatergic and GABAergic neurons restores the excitatory/inhibitory balance after injury. In addition, transient populations of injury-responsive neurons (iNeurons) show elevated plasticity between 1 and 3 weeks post-injury. Using cross-species transcriptomics and CRISPR/Cas9 mutagenesis, we found iNeurons are injury-surviving neurons that share transcriptional similarities with a rare population of spontaneously plastic mouse neurons. iNeurons are required for functional recovery and employ vesicular trafficking as an essential mechanism that underlies neuronal plasticity. This study provides a comprehensive resource of the cells and mechanisms that direct spinal cord regeneration and establishes zebrafish as a model of plasticity-driven neural repair.

INTRODUCTION

Mammalian spinal cord injuries (SCI) elicit complex multi-cellular responses that impede regeneration and cause permanent functional deficits in mammals (He and Jin, 2016; Brennan and Popovich, 2018; Sofroniew, 2018; Milich et al., 2019; Fouad et al., 2021; Tran et al., 2022). Anti-regenerative neuron-extrinsic factors comprise chronic inflammation, fibrotic scarring, demyelination and the acquisition of a regeneration restricting extracellular milieu. These injury complications exacerbate the inherently limited ability of the mammalian spinal cord (SC) to replenish lost neurons via adult neurogenesis or to regrow lesioned axon tracts. Consequently, even the most groundbreaking regenerative therapies targeting select cell types or individual molecules have only yielded modest improvement in cellular and functional outcomes (Park et al., 2008; Sofroniew, 2018). SCI studies have since pursued combinatorial strategies as a more promising therapeutic avenue (DePaul et al., 2017; Anderson et al., 2018; Nakamura et al., 2021). We propose that comprehensive and simultaneous examination of neuronal and non-neuronal cells after SCI is fundamental to understanding and manipulating the multi-cellular complexities of neural injuries.

Unlike mammals, adult zebrafish have an innate ability to spontaneously recover from severe SCI. Following complete transection of SC tissues, zebrafish reverse paralysis and regain swim function within 6 to 8 weeks of injury (Mokalled et al., 2016; Burris et al., 2021). Pro-regenerative injury responses involving immune and progenitor cells, neurons and glia, cooperate to achieve spontaneous and efficient repair in zebrafish (Reimer et al., 2008; Kuscha et al., 2012; Briona et al., 2015; Cavone et al., 2021; Klatt Shaw et al., 2021; Vandestadt et al., 2021; Saraswathy et al., 2022). Early after SCI, potent populations of progenitor cells, including central canal-surrounding ependymo-radial glial cells (ERGs), are activated to replenish lost neurons and glia (Reimer et al., 2008; Briona et al., 2015; Klatt Shaw et al., 2021; Saraswathy et al., 2022). Newly differentiated motor neurons and interneurons populate the regenerate tissue, as pre-existing neurons regrow axons across lesioned tissues (Reimer et al., 2008; Kuscha et al., 2012; Saraswathy et al., 2022). Though less studied, glial cells are thought to enact instrumental pro-regenerative responses throughout the course of regeneration (Goldshmit et al., 2012; Mokalled et al., 2016; Klatt Shaw et al., 2021). Bridging glia extend cellular bridges across the lesion and oligodendrocytes direct remyelination, in addition to glial support of neuronal survival and functions. However, a holistic understanding of the cellular interactions that coordinate the pro-regenerative responses to direct SC regeneration in zebrafish is to be acquired.

The advent of single-cell transcriptomics provided the tools to achieve a refined understanding of molecular SCI responses across species and cell types. Multiple single-cell RNA sequencing (scRNA-seq) atlases have been generated for mouse SCI, rat SCI or human SC tissues (Milich et al., 2021; Matson et al., 2022; Yao et al., 2022; Rodrigo Albors et al., 2023; Yadav et al., 2023). Single-cell studies from mice revealed new insights into macroglial cell-cell interactions after injury, revealed a rare population of lumbar spinocerebellar neurons that elicit a regeneration signature, or characterized the responses of astrocytes after injury (Milich et al., 2021; Hou et al., 2022; Matson et al., 2022; Rodrigo Albors et al., 2023). However, single-cell studies from zebrafish SC tissues have been limited to isolated immune or progenitor motor neuron cells and to larval stages (Cavone et al., 2021; Scott et al., 2021). Thus, a complete resource of the regenerative cells and mechanisms from adult zebrafish is required to develop a molecular understanding of the cell identities that enable or limit spontaneous plasticity and regeneration.

The fundamental principles that determine or limit regenerative capacity across species have eluded scientists for ages. While pro-regenerative injury responses are overwhelmed by anti-regenerative complications in mammals, zebrafish cells exhibit increased potency and exclusively pro-regenerative signatures after SCI. Molecular and cellular studies of select cell types or regenerative pathways revealed key insights into the cellular contributions and molecular signatures associated with elevated regenerative capacity. Specifically, while ependymal cells elicit limited stem cell potential in adult mice (Ren et al., 2017; Shah et al., 2018), zebrafish ERGs retain radial glial features and contribute to neurogenesis and gliogenesis after SCI (Reimer et al., 2008; Briona et al., 2015; Klatt Shaw et al., 2021; Saraswathy et al., 2022). The disparities in neuron progenitor capacities between zebrafish and mammals yielded an assumption that neurogenesis-based neural repair is unachievable in mammals and directed the community's efforts toward plasticity-based neural repair strategies. However, while zebrafish has been an established model of neuron regeneration, it remains unclear whether zebrafish could contribute insights and applications into plasticity-driven repair mechanisms. Thus, how and why neuronal injury responses differ between zebrafish and mammals require comprehensive molecular investigation and cross-species comparisons.

This study presents an atlas of the dynamic responses across major spinal cell types during early, intermediate and late stages of regeneration in adult zebrafish. Single nuclear RNA sequencing (snRNA-seq) was performed at 0, 1, 3 and 6 weeks post-injury. Neurons elicit elevated signaling activity relative to the dozens of cell types that respond to injury. While SCI

disrupts the excitatory/inhibitory neuron balance, sequential neurogenesis of excitatory and inhibitory neurons restores the homeostatic neuronal landscape at late stages of regeneration. In addition to regenerating new neurons, a transient regenerative signature emerges in a population of injury-responsive neurons (iNeurons) between 1 and 3 weeks post-injury. iNeurons are transcriptionally analogous to a rare population of mouse neurons that show spontaneous plasticity after injury (Matson et al., 2022). iNeuron markers genes are required for functional SC repair, and dynamic vesicular trafficking is a central mechanism that promotes spontaneous neuronal plasticity. This study identifies multi-layered modes of regenerative neurogenesis and neuronal plasticity during innate spinal cord regeneration, and establishes zebrafish as a platform to identify and manipulate regeneration- and plasticity-based modes of neural repair.

RESULTS

Molecular identification and temporal dynamics of cell types during SC regeneration.

To determine the transcriptional identities of the cells that directs successful SC regeneration, we performed complete SC transections on adult zebrafish and dissected 3 mm sections of SC tissues surrounding the lesion site at 1, 3, and 6 weeks post-injury (wpi) for nuclear isolation. Corresponding tissue sections were collected from uninjured controls. SC tissues were pooled from 50 animals per time point, and 2 pools of independent biological replicates were analyzed for each time point. Our dataset spans key regenerative windows including early injury-induced signals at 1 wpi, neuronal and glial regeneration at 3 wpi, and cellular remodeling at late stages of regeneration at 6 wpi (Mokalled et al., 2016). Isolated nuclei were sequenced using 10x genomics platform (3' v3.1 chemistry) and a total of 73,814 nuclei were obtained (Matson et al., 2018). Nuclei were subsequently filtered to exclude droplets that included no nuclei or nuclei doublets before proceeding with downstream analysis using the Seurat package (Fig. 1A and S1A-C).

Clustering of SC nuclei revealed 41 cell clusters with distinct molecular identities and temporal dynamics (Fig. S1D). Postulating that previously established cell type classifiers are likely biased toward cell identities present the mammalian nervous system or in developing zebrafish, we optimized cell type identification by generating a custom-assembled Vertebrate CNS Marker (VNM) database. VNM compiled cell type markers commonly present in the central nervous system from over 12 datasets and vertebrate species including zebrafish, mice, and humans (Guillemot, 2007; Zhang et al., 2014; Lu et al., 2015; Hernandez-Miranda et al., 2017; Tang et al.,

2017; Haring et al., 2018; Hayashi et al., 2018; Rosenberg et al., 2018; Sathyamurthy et al., 2018; Zeisel et al., 2018; Baek et al., 2019; Rougeot et al., 2019; Tambalo et al., 2020; Cavone et al., 2021; Milich et al., 2021). We then cross-referenced the differentially expressed (DE) markers for each cluster with our VNM database (Table S1 and Fig. S1E). Scoring matrix heatmap from this analysis identified 8 major cell types comprising neurons, glia/ERGs, oligodendrocyte precursor cells (OPCs), oligodendrocytes, leukocytes, pericytes and endothelial cells, in addition to one cell cluster of undetermined identity (Fig. 1B and S1E). VNM-based cell type classification was further confirmed by evaluating the expression of canonical marker genes for each cluster (Fig. 1C). *elavl4* and *snap25a* were enriched in neurons, *gfap* and *slc4a10a* in glia/ERGs, *cspg4* and *sema5a* in OPCs, *mpz* and *mbpa* in oligodendrocytes, *lgals9l1* and *ptprc* in leukocytes, *col1a1b* and *col1a1a* in pericytes, and *igfr1b* and *col4a1* in endothelial cells (Fig. 1C). Although these canonical markers were enriched in their respective clusters, the proportions of cells expressing *lgals9l1* and *ptprc* in leukocytes, *col1a1b* and *col1a1b* in pericytes, and *igfr1b* and *col4a1* in endothelial cells were relatively small. We conclude that our VNM database is likely still biased toward commonly used mammalian cell markers that are not necessarily the best markers for adult zebrafish, and that our single-cell atlas provides a platform to identify improved CNS markers for adult zebrafish cells. To test this hypothesis, we examined whether our snRNA-seq dataset identified improved cell-specific DE markers in adult zebrafish SCs (Fig. 1F). Glia/ERG cells expressed the cilia-associated *cfap57* gene, indicative of the ciliated nature of the SC central canal-lining ERGs. Leukocytes were enriched for *mrc1b* and *slco2b1* genes along with the cell adhesion molecule coding *mcamb* gene. Finally, pericytes (expressing *ahnak, plpp3* and *ctgfb*) and endothelial cells (expressing *pxdn* and *bcam*) shared several DE markers including the collagen family gene *col4a1*. These studies indicated that extrapolating mammalian CNS or developmental zebrafish markers requires validation, and provided a platform to identify new and improved CNS cell markers in adult zebrafish.

To examine the temporal dynamics of SC cells during regeneration, we determined the numbers and relative proportions of nuclei within each coarse cluster in the integrated dataset (Fig. 1D-E and S1F-G). Neurons comprised 39% of the nuclei harvested from uninjured SCs, but their proportion decreased to 18% at 1 wpi and recovered to 27% at 6 wpi. Expectedly, the proportions of leukocytes increased from 11% of total nuclei prior to injury to 23% at 1 wpi and gradually decreased to 15% at 6 wpi. We observed an expansion in the relative abundance of glia/ERGs between 1 and 3 wpi, whereas OPCs maintained similar proportions at all timepoints. Pericytes and endothelial cells comprised 1.3% and 0.9% of uninjured nuclei, and their

127 proportions increased to 1.7% and 2.3% of total nuclei at 1 wpi, respectively. These studies
128 provided a comprehensive resource of the cellular architecture that directs successful SC repair
129 and revealed a gradual recovery in neuronal proportions during innate SC repair.

130 **Neurons are active signaling hubs during spinal cord regeneration.**

131 To infer molecular modes of intercellular communication during SC regeneration, we surveyed
132 signaling pathways that are differentially active between 0 and 6 wpi (Fig. 2 and S2). We first
133 converted our dataset of zebrafish genes to their human orthologues using the BioMart package
134 from Ensembl. The CellChat R package was then used to quantitatively analyze global
135 intercellular communication networks based on the expression of ligands, receptors and cofactors
136 (Jin et al., 2021). In control SC tissues, the cumulative strengths of outgoing signaling pathways
137 were highest in neurons and OPCs relative to other cell types, indicating active signaling in
138 neurons and glia under homeostatic conditions (Fig. 2A-B). After SCI, the cumulative strengths of
139 outgoing signaling increased in all cell types, indicating tissue-wide responses are activated after
140 injury (Fig. 2A-B). The strengths of outgoing signaling pathways from endothelial cells and
141 pericytes peaked at 1 wpi, whereas signaling from oligodendrocytes was highest at 6 wpi (Fig.
142 2A-B). These results are consistent with early activation of endothelial cells and pericytes after
143 injury, and support a later role for oligodendrocytes during remyelination of regenerating axons.
144 Notably, outgoing signaling from neurons was elevated across all time points and increased 2.5-
145 fold between 0 and 6 wpi (Fig. 2A-B). Incoming signaling strengths received by neurons also
146 increased 2.5-fold between 0 and 6 wpi (Fig. S2A-B). Incoming signaling received by OPCs was
147 highest among spinal cell types across all time points (Fig. S2A-B). Confirming our CellChat
148 analysis, trajectory inference analysis showed OPCs and neurons, along with glia/ERGs and
149 oligodendrocytes, have elevated transcriptional activity during SC regeneration (Gulati et al.,
150 2020) (Fig. S2C). Mapping of ligand-receptor interactions predicted cell-cell signaling interactions
151 are highest between neurons and OPCs (Fig. 2C). These results indicated neurons and OPCs
152 have elevated and dynamic transcriptional and signaling activities during zebrafish SC
153 regeneration.

154 **Global and neuron-specific analyses of injury-induced signaling pathways.**

155 Global CellChat analysis revealed 25 to 29 active signaling pathways in control, 3 and 6 wpi SC
156 tissues. The highest number of signaling pathways (35 pathways) were enriched at 1 wpi,
157 indicating abundant and dynamic intercellular communication during early stages of SC
158 regeneration (Fig. 2D). Overall, 13 pathways were enriched at 1, 3 or 6 wpi relative to uninjured

159 controls, and 5 of the 13 injury-induced pathways were specifically induced at 1 wpi. Globally-
160 induced signaling pathways included cell adhesion signaling networks (L1CAM, JAM3, CNTN1
161 and EPHA2/3/4/5), extracellular matrix (ECM) mediated signaling networks (TENASCIN, PSAP,
162 FN1, MDK, SEMA3A/B/C, ENTPD1 and HSPG2) and developmental signaling pathways (BMP7
163 and NOTCH1/2/4) (Fig. 2D).

164 To identify molecular pathways that account for elevated neuron signaling, we focused our
165 subsequent analysis on signaling pathways predicted to be outgoing from or incoming into
166 neurons (Fig. 2E and S2D). For outgoing signaling, 17 to 22 pathways were predicted to be
167 activated by neurons between 0 and 6 wpi. In addition to homeostatic signaling pathways
168 increasing in strengths after injury, 6 pathways were injury-induced and 4 out of the 6 injury-
169 induced pathways were specific to 1 wpi neurons (Fig. 2E-F). Cell adhesion molecules mediate
170 the cell-cell and cell-ECM interactions necessary for cell survival, migration, synaptogenesis and
171 axon guidance during regeneration (Walsh and Doherty, 1996; Zhang et al., 2008). Specifically,
172 the L1 cell adhesion molecules (L1CAM) are members of the immunoglobulin superfamily of cell
173 adhesion molecules that were previously shown to be upregulated in axons after CNS injury
174 (Bernhardt et al., 1996; Jung et al., 1997; Zhang et al., 2008). We found that L1CAM signaling is
175 highly active in neurons and glial cells, suggesting L1CAM plays neuronal and axon-independent
176 regenerative roles (Fig. 2F). Ephrin A (EPHA) signaling, which is best studied for its role in cell
177 adhesion, positioning and migration, is activated between neurons, OPCs and pericytes after
178 injury (Fig. 2F). The cell adhesion molecule Contactin-1 (CNTN-1) interacts with NRCAM (data
179 not shown), mediating signaling crosstalk between neurons, glia/ERGs and endothelial cells
180 (Haenisch et al., 2005; Mikami et al., 2009) (Fig. 2F). By providing either permissive or non-
181 permissive microenvironments after injury, growth factors and ECM components play crucial
182 regenerative roles after SCI. Tenascins are matricellular proteins that modulate cell adhesion,
183 migration and growth (Busch and Silver, 2007). We found TENASCIN signaling, mediated by
184 TENASCIN-R (TNR) and the integrins ITGAV and ITGB6 (data not shown), is a major neuron-
185 and OPC-derived pathway that converges onto endothelial cells after SCI (Fig. 2F). These studies
186 revealed complex multicellular communication networks that coordinate signaling between
187 neurons, glia non-neural injury-responding cells during SC repair.

188 **Neuronal E/I balance is restored during successful SC regeneration.**

189 To explore the cellular dynamics that support neuronal and functional recovery after zebrafish
190 SCI, we examined neuronal cell types and states prior to and after injury. Subcluster analysis

191 identified 30 distinct neuron clusters between 0 and 6 wpi (Fig. 3A and S3A-B). Balanced synaptic
192 excitatory and inhibitory (E/I) transmission is a central feature of CNS function as altered E/I
193 balance results in severe behavioral defects in humans (Isaacson and Scanziani, 2011). Despite
194 eliciting features of cellular regeneration, SCI in mouse neonates causes impaired locomotor
195 recovery due to imbalanced E/I transmission (Dudek and Sutula, 2007; Gao and Penzes, 2015;
196 Bertels et al., 2022). With zebrafish recovering swim function after SCI, we postulated that
197 balanced E/I transmission is a feature of functional SC repair in zebrafish. To test this hypothesis,
198 we first performed a bioinformatic characterization of the excitatory and inhibitory neurotransmitter
199 properties of the neuron clusters identified in our dataset (Fig. 3B). Neuron classification was
200 based on the expression of classical markers of excitatory (slc*17a6a, slc17a6b*), inhibitory
201 (*slc6a5, gad1a, gad1b, gad2*) and cholinergic (*chata, slc5a7a*) neurons (Fig. S4C). Neuron
202 subclusters were classified as excitatory, inhibitory, cholinergic, excitatory/cholinergic, and
203 inhibitory/cholinergic (Fig. 3B and S3C-E). The proportions of excitatory (13.9%) was lower than
204 inhibitory (36.1%) neurons in uninjured SC tissues (Fig. 3C), resulting in a baseline E/I ratio of 0.4
205 (Fig. 3D). The profile of excitatory neurons rapidly increased to 21.1% of total neurons at 1 wpi
206 and stabilized at 21.6% at 2 wpi (Fig. 3C). Inhibitory neurons accounted for 48.6% of total neurons
207 at 1 wpi and continued to expand to 59.4% at 2 wpi (Fig. 3C). By 6 wpi, the relative proportions
208 of excitatory and inhibitory neurons returned to near baseline levels, accounting for 16 and 42.2%
209 of total neurons, respectively (Fig. 3C). Bioinformatic calculation of the E/I ratio confirmed an
210 imbalance toward an excitatory phenotype at 1 wpi and a recovery to baseline levels by 6 wpi
211 (Fig. 3D).

212 To validate our bioinformatic E/I balance calculations *in vivo*, we generated dual transgenic
213 reporter fish that simultaneously label glutamatergic excitatory neurons (*vglut2a*:RFP) and
214 GABAergic inhibitory neurons (*gad1b*:GFP) (Satou et al., 2013). Complete SC transections were
215 performed on double transgenic animals and SC tissues were collected for histological
216 examination at 0, 1, 3 and 6 wpi (Fig. 3E-F). Absolute numbers and relative proportions of RFP-,
217 GFP- and HuC/D-expressing neurons were quantified in SC cross sections at 450 μm rostral to
218 the lesion as a proxy evaluation of the E/I landscape during regeneration. Compared to control
219 SC tissues, the profiles of *vglut2a*$^+$ excitatory neurons (*vglut2a*$^+$ HuC/D$^+$) doubled in proportion at
220 1 wpi and were maintained near 1 wpi levels until 6 wpi (Fig. 3G and S3F). On the other hand,
221 the profiles of *gad1b*$^+$ inhibitory neurons (*gad1b*$^+$ HuC/D$^+$) gradually increased by between 1 and
222 6 wpi relative to controls (Fig. 3H and S3G). Notably, the absolute numbers of HuC/D$^+$ neurons
223 drastically increased at 1 and 3 wpi, indicating extensive neuronal remodeling during SC

224 regeneration (Fig. S3H). Thus, consistent with our snRNA-seq findings, these *in vivo* studies
225 confirmed an early surge in excitatory neurons at 1 wpi and a recovery of the E/I balance toward
226 baseline levels by 6 wpi (Fig. 3I).

227 **Neurogenesis of excitatory and inhibitory neurons after SCI.**

228 We next explored the cellular bases behind the recovery of E/I balance during zebrafish SC repair.
229 The observed E/I ratio changes could be due to sequential neurogenesis of excitatory then
230 inhibitory neurons after SCI. Alternatively, E/I ratios could reflect plasticity and changes in the
231 neurotransmitter properties of pre-existing neurons. To distinguish between these possibilities,
232 we first performed a cell proliferation assay. Dual transgenic fish for *vglut2a*:RFP and *gad1b*:GFP
233 were subjected to SCI and a single EdU pulse for 24 hrs prior to SC tissue collection. SC tissues
234 were harvested at 1, 3 and 6 wpi for co-labelling with the proliferation marker EdU (Fig. 4A-B and
235 S4A). SC tissues from uninjured animals that received a single EdU injection for 24 hrs were
236 harvested as controls. In striking manifestation of the regenerative capacity of zebrafish SC
237 tissues after SCI, EdU incorporation was markedly elevated at 1 wpi relative to 0, 3, and 6 wpi
238 (Fig. 4C and S4B). The profiles and absolute numbers of newly generated glutamatergic neurons
239 (*vglut2a*$^+$ EdU$^+$) peaked at 1 wpi relative to control, 3 or 6 wpi SC sections (Fig. 4D and S4C),
240 supporting a surge of regenerating excitatory neurons at 1 wpi. As the profiles of GABAergic
241 neurons showed a gradual increase up to 6 wpi (Fig. 3H) and due to low numbers of EdU$^+$ cells
242 at 3 and 6 wpi, we were unable to evaluate the profiles of newly generated GABAergic neurons
243 with a single EdU pulse (Fig. 4E and S4D).

244 To overcome this limitation and evaluate the numbers of regenerating glutamatergic and
245 GABAergic neurons after SCI, we performed SC transections on *vglut2a*:RFP and *gad1b*:GFP
246 dual transgenic fish followed by daily EdU injections for 1 or 3 wpi (Fig. 4F-G and S4E). Uninjured
247 control animals received daily EdU injections for 1 week prior to SC tissue collection. Compared
248 to single EdU pulses, daily EdU labeling allowed us to estimate the total and cumulative profiles
249 of regenerating neurons. To account for anatomical differences along the proximo-distal axis of
250 lesioned SC tissues, RFP-, GFP- and EdU-expressing cells were quantified from SC sections
251 150, 450 and 750 μm rostral to the lesion. The numbers and proportions of EdU$^+$ cells sharply
252 increased at 1 wpi and showed less pronounced additive EdU incorporation at 3 wpi (Fig. S4F-
253 G). The profiles of newly formed glutamatergic (EdU$^+$ *vglut2a*$^+$) neurons markedly increased at 1
254 and 3 wpi relative to controls (Fig. 4H and S4H). The profiles of regenerating GABAergic (EdU$^+$
255 *gad1b*$^+$) neurons were significantly elevated at 1 wpi compared to controls, and continued to

256 increase at 3 wpi compared to 1 wpi (Fig. 4I and S4I). As proximal tissue sections (150 μm from
257 lesion) showed elevated neurogenesis across time points, differential dynamics of glutamatergic
258 and GABergic neuron regeneration were most prominent in more distal SC sections (750 μm from
259 lesion) (Fig. 4H and 4I). At these levels, the profiles of newly formed glutamatergic (EdU$^+$ *vglut2a*$^+$)
260 neurons sharply increased at 1 wpi and maintained comparable presence at 3 wpi (Fig. 4H),
261 whereas GABAergic (EdU$^+$ *gad1b*$^+$) continuously increased from 1 to 3 wpi (Fig. 4I). Together,
262 these *in vivo* studies showed glutamatergic neurogenesis precedes a continuous and slower
263 regeneration timeline for GABAergic neurons, suggesting that sequential neurogenesis of
264 different neuron subtypes around the lesion accounts for the dynamic changes in E/I properties
265 during zebrafish SC regeneration.

266 **Identification of injury-responsive iNeurons during SC regeneration.**

267 To delve into the distribution of specific neuron subclusters prior to and after SCI, we calculated
268 the numbers and relative proportions of each neuron subcluster between 0 and 6 wpi (Fig. 3A
269 and S3A-B). Out of the 30 neuron types subclustered from our integrated dataset, 2 subclusters
270 (neuron subclusters N18 and N22) were exclusively present after injury and are referred to
271 hereafter as injury-responsive neurons or iNeurons (Fig. 5A and S5A). Our analysis retrieved
272 equal numbers of N18 and N22 iNeurons at 1 wpi (Fig. 5A). The number and proportion of N18
273 iNeurons gradually decreased between 1 and 6 wpi. Conversely, N22 iNeurons were sharply
274 depleted by 85% at 3 wpi and not detectable at 6 wpi (Fig. 5A). DE marker analysis identified
275 *ebf2, gdf11, lhx4* and *kidins220a* as N18 iNeuron markers but failed to determine a clear
276 transcriptional signature that distinguishes N18 iNeurons from other neuron clusters (Fig. 5B). On
277 the other hand, in support of a pro-regenerative role for N22 iNeurons, *atf3* and *sox11b* were
278 specifically enriched in N22 iNeurons (Fig. 5C). *atf3* and *sox11b* are known markers and drivers
279 of neuronal survival and axon regrowth in zebrafish and mice (Jankowski et al., 2009; Jing et al.,
280 2012; Wang et al., 2015; Gey et al., 2016; Wang et al., 2017; Kole et al., 2020). By gene ontology
281 (GO) analysis, functional terms associated with axon development and regrowth, synaptic activity
282 and vesicular trafficking were highly enriched in N22 iNeurons (Fig. 5D). These findings indicated
283 N22 iNeurons comprise a transient subpopulation of injury-responsive neurons that contributes
284 to functional SC repair.

285 **iNeurons are signaling hubs during SC regeneration.**

286 To evaluate the role of N22 iNeurons during SC regeneration, we determined the extent and
287 identities of the signaling pathways that are initiated and received by N22 iNeurons using

288 CellChat. To specifically identify N22 iNeurons within the rest of the SC microenvironment, we
289 first tracked and identified N22 iNeurons in the integrated dataset that includes all SC cells (Fig.
290 S5A). Clusters 5 and 21 from the integrated dataset accounted for the majority of N22 iNeurons
291 and were renamed iNeurons for CellChat analysis (Fig. S5B). Strikingly, compared to the global
292 cell-interactions derived from the integrated dataset (Fig. 5E), the cumulative and reciprocal
293 signaling strengths were highest between iNeurons and OPCs at 1 wpi (Fig. 5F). The cumulative
294 strengths of outgoing and incoming signaling were markedly lower in the rest of the neuronal cells
295 compared to iNeurons (Fig. 5F and S5C).

296 To examine the molecular features of the crosstalk between iNeurons and OPCs, we identified
297 major signaling networks that are either incoming or outgoing from iNeurons (Fig. 5F and S5D).
298 CellChat analysis showed iNeurons have a high probability to transduce SEMA5 and NRXN3
299 signaling into OPCs and other neurons, respectively (Fig. 5F). NRX3, CDH4 and CADM1
300 signaling were also identified as highly probably incoming and outgoing iNeuron signals (Fig. 5F
301 and S5D). Consistent with the gene ontology of N22 iNeuron genes (Fig. 5B), we observed a high
302 probability for reciprocal Neuregulin (NRG)-ERBB signaling between iNeurons and OPCs at 1 wpi
303 (Fig. 5F and S5D). ErbB signaling was recently shown to regulate OPC transformation and
304 spontaneous remyelination after SCI in mice (Bartus et al., 2019). We found NRG2 and NRG3
305 ligands expressed by OPCs are the most probable activators of the ERBB4 receptor expressed
306 in iNeurons (Fig. 5F). Reciprocally, there are several interaction probabilities for the NRG1/2/3
307 and ERBB2/4 as outgoing signaling ligands from iNeurons to OPCs (Fig. S5D). These results
308 showed iNeurons are potent centers of molecular signaling during SC regeneration, and
309 suggested that reciprocal signaling between iNeurons and OPCs is a central feature of innate SC
310 repair.

311 **Cross-species comparisons between zebrafish and mouse neurons.**
312 To explore potential similarities and differences between zebrafish and mouse neurons after SCI,
313 we integrated our neuronal snRNA-seq data with a recently published dataset that dissected the
314 transcriptional identities of mouse neurons after SCI (Matson et al., 2022). Notably, Matson *et al.*
315 identified a rare population of mouse SC neurons that express regeneration associated genes
316 (RAG) after injury and that are referred to hereafter as RAG neurons (or *Mm*_RAG neurons)
317 (Matson et al., 2022). Gene expression in the RAG cluster included *Atf3* and *Sox11*, suggesting
318 mouse RAG neurons and zebrafish iNeurons may have similar transcriptional profiles. To
319 integrate the transcriptomic datasets for mouse SCI (Gene Expression Omnibus GSE172167)

320 with our zebrafish snRNA-seq dataset, we first converted our zebrafish genes to their mouse
321 orthologues using BioMart of Ensemble, then identified neuronal cell populations from both
322 datasets before proceeding with cross-species integration. Subclustering of integrated mouse and
323 zebrafish neurons revealed 45 different clusters (referred to hereafter as ZM clusters) with
324 different dynamic distributions across timepoints and species (Fig. 6A-B and S6). UMAP plot and
325 cell numbers across all time points showed that 46.6% of neuronal ZM clusters were
326 overwhelmingly populated by both mouse and zebrafish neurons (at least 50 cells from each
327 species) (Fig. 6B and S6A). 28.9% of ZM clusters comprised fish-only clusters (ZM3, 10, 17, 28,
328 30, 31, 32, 34, 37, 39, 40, 43 and 44), with 24.4% of ZM clusters including mouse-only clusters
329 (ZM6, 9, 16, 26, 27, 33, 35, 36, 38, 41 and 42). These studies underscored differences and
330 similarities between the transcriptional landscapes of zebrafish and mouse neurons after SCI.

331 To identify zebrafish iNeurons and mouse RAG cells within the integrated ZM dataset, we
332 examined the expression of top iNeuron and RAG DE markers in the integrated dataset. *atf3,*
333 *sox11, gap43, vamp4, syt11, hdac10* and *mthfd1l* were used for zebrafish iNeuron classification.
334 *Atf3, Sox11, Gap43, Sprrr1a, Tnfrs12a, Klf6, Bdnf* and *Adcyap1* were used for mouse RAG
335 identification. Markers that are common to both iNeurons and RAG cluster (*atf3*, *sox11* and
336 *gap43*) were enriched in cluster ZM20 (Fig. 6C-E). RAG cluster markers (*Tnfrsf12a, Bdnf, Klf6*
337 and *Adcyap1*) and iNeuron markers (*Vamp4, Hdac10, and Mthfd1l*) were also enriched in cluster
338 ZM20 (Fig. 6C). By tracing the identities of zebrafish iNeurons within our integrated ZM dataset,
339 50% of zebrafish iNeurons mapped to cluster ZM20 (Fig. 6D). The numbers of proportions of
340 ZM20 cells peaked at 1 wpi in zebrafish and between 1 and 3 wpi in mice (Fig. 6E and S6B).
341 Mapping iNeuron and RAG cells within cluster ZM20 showed these two populations were
342 adjacently situated in the UMAP plot and did not split into separate clusters at higher resolution,
343 indicating their transcriptional similarity (Fig. 6F). DE marker comparisons verified the
344 transcriptional similarities between N18 iNeurons, N22 iNeurons and mouse RAG neuron markers
345 (Fig. 6G). Gene ontology analysis showed that zebrafish iNeurons and mouse RAG clusters are
346 significantly enriched with shared pro-regenerative GO terms including axon guidance, synapse
347 organization and vesicular trafficking (Fig. 6H). These findings indicated that zebrafish iNeurons
348 and mouse RAG neurons clustered into the ZM20 cluster following cross-species data integration,
349 and suggested zebrafish iNeurons and mouse RAG cells share transcriptional and functional
350 similarities.

351 ***in vivo* mapping of iNeurons during SC regeneration.**

352 To validate the emergence of an iNeuron transcriptional signature in regenerating SC tissues, we
353 performed HCR *in situ* hybridization for select markers that are uniquely expressed in N22
354 iNeurons and compared to all other spinal types in the integrated dataset (Fig. 5C). To enable
355 differential labeling of regenerating and pre-existing neurons, wild-type fish were subjected to SCI
356 and daily EdU injections. *syt11b* and *vamp4* HCR *in situ* hybridization and staining for HuC/D and
357 EdU were performed at 0, 1 and 3 wpi (Fig. 7A and 7D). To test whether iNeuron markers are
358 preferentially expressed in neurons, integrated densities of their HCR *in situ* hybridization signals
359 were quantified in total SC tissues and in HuC/D$^+$ neurons (Fig. 7A-F and S7A-H). At 1 wpi,
360 *synaptotagmin XI b (syt11b)* expression increased by 3.6-fold in total SC tissues and by 4.3-fold
361 in HuC/D$^+$ neurons (Fig. 7B-C). *syt11b* expression was reduced to its wild-type level by 3 wpi (Fig.
362 7B-C). Expression of vesicle-*associated membrane protein 4 (vamp4)* was upregulated at 1 and
363 3 wpi, with 2.3- to 2.5-fold increase in total SC tissues and HuC/D$^+$ neurons at 1 wpi (Fig. 7E-F).
364 Since *syt11b* showed robust expression and upregulation in neurons and to address putative
365 redundancy between the *syt11b* and *syt11a* paralogs, we examined *syt11a* expression after SCI
366 (Fig. S7A-E). Like *syt11b*, *syt11a* transcripts were upregulated after injury, including in neurons.
367 However, unlike *syt11b*, *syt11a* expression was not restricted to neurons including expression in
368 ependymal cells surrounding the central canal at 1 wpi (Fig. S7E). These findings validated *syt11b*
369 and *vamp4* as markers of zebrafish iNeurons during spinal cord regeneration.

370 **iNeurons are surviving neurons that elicit spontaneous plasticity after injury.**
371 The emergence of an iNeuron transcriptional profile at 1 wpi raised a central question related to
372 the origin of their pro-regenerative signature. We postulated that iNeurons could either represent
373 newly formed regenerating, or a population of spontaneously plastic neurons that survive injury
374 and support immediate repair. To distinguish between these hypotheses, we quantified the
375 profiles of iNeurons that express *syt11b/a*, HuC/D and EdU (Fig. 7G-I and S7A-H). In these
376 experiments, HuC/D$^+$ EdU$^+$ represent regenerating neurons and HuC/D$^+$ EdU$^-$ represent pre-
377 existing neurons. Expectedly, the profiles of regenerating neurons significantly increased from 1
378 to 3 wpi, indicating potent neurogenic responses are activated during innate SC repair (Fig. 7H).
379 At 1 wpi, *syt11b* transcripts labeled 14.5% of HuC/D$^+$ neurons (Fig. 7G), and only 6.4% of
380 regenerating neurons (Fig. 7I). Even though *syt11a* labels slightly higher proportion of neurons
381 (21.85%) at 1 wpi, more than 90% of the newly generated neurons don't show expression of
382 *syt11a* (Fig. S7C-E). These results indicated that over 90% of iNeurons are pre-existing neurons
383 that survive SCI.

384 Since the majority of iNeurons are pre-existing in control SC tissues, we examined whether
385 iNeurons represent a specific population of neurons with elevated survival capacity or
386 spontaneous plasticity. To address this question, we performed *syt11b* HCR *in situ* hybridization
387 on *vglut2a*:RFP and *gad1b*:GFP dual transgenic fish, which label glutamatergic excitatory and
388 GABAergic inhibitory neurons, respectively (Fig. 7J). Neuron subtypes not labeled with
389 *vglut2a*:RFP or *gad1b*:GFP were labeled as others. The integrated density of *syt11b* transcript
390 signals broadly increased at 1 wpi (Fig. S7I), including upregulated expression in *vglut2a*$^{+}$ and
391 *gad1b*$^{+}$ neurons at 1 wpi (Fig. S7J-K). Notably, only 37.5% and 20.7% of the combined *syt11b*
392 signal was found in glutamatergic and GABAergic neurons at 1 and 2 wpi, respectively, indicating
393 that "other" neuron subtypes express the majority of *syt11b* during regeneration (Fig. 7K). These
394 findings indicated that iNeurons do not represent a specific neuron subtype, and suggested that
395 multiple zebrafish neurons survive SCI and elicit an iNeuron transcriptional and regenerative
396 signature during early stages of SC repair.

397 **iNeurons marker genes are required for cellular and functional recovery after SCI.**
398 To evaluate the roles of iNeuron marker genes during SC regeneration, we employed
399 CRISPR/Cas9 mutagenesis, SCI and functional swim assays (Fig. 8A) (Burris et al., 2021; Klatt
400 Shaw and Mokalled, 2021). Among the top DE markers of N22 iNeurons, 10 genes were filtered
401 as iNeuron-specific and chosen for mutagenesis (*hdac10, mthfd1l, si:ch211-153j24.3, fhdc5,*
402 *shootin3, syt11b, fam171b, chrnb2b, fblim1, vamp4*) (Fig. 5C). *atf3* was selected as a positive
403 control (Wang et al., 2017). In addition to targeting *syt11b*, we individually and combinatorially
404 targeted the *syt11a* and *syt11b* paralogs to account for putatively redundant effects on
405 regeneration. For efficient and simultaneous gene targeting in zebrafish, we used a recently
406 adapted CRISPR/Cas9 protocol that achieves near complete mutagenesis in F0 injected adults
407 (Burris et al., 2021; Klatt Shaw and Mokalled, 2021). CRISPR/Cas9 targeted animals (crispants)
408 were raised to adulthood and mutagenesis rates were examined by capillary electrophoresis (Fig.
409 S8A). Adult crispants with >90% mutagenesis were subjected to SCI, and swam against
410 increasing water current inside an enclosed swim tunnel to screen for functional regeneration
411 defects. At 4 wpi, swim endurance was significantly reduced in *atf3* and *vamp4* crispants (Fig.
412 8B). Targeting *syt11a and syt11b* paralogs individually did not alter swim endurance. However,
413 swim endurance was diminished in *syt11a;syt11b* dual crispants, indicating the *syt11* paralogs
414 were functionally redundant during SC repair (Fig. 8B). To validate swim capacity defects in
415 iNeuron gene crispants, we tracked the swim behavior of *atf3*, *vamp4* and *syt11a;syt11b* crispants
416 under at 0, 10 and 20 10 cm/sec current velocities (Fig. 8C). Compared to uninjected control

417 siblings and in the absence of water flow, swim distance was 50-55% reduced in *atf3* and
418 *syt11a;syt11b* crispants and 25% reduced in *vamp4* crispants (Fig. 8C). Swim distance was
419 significantly lower in *atf3*, *vamp4* and *syt11a/b* at 10 and 20 cm/sec water current velocities (Fig.
420 8C). These results indicated the iNeuron markers *atf3*, *vamp4* and *syt11a/b* are required for
421 functional SC repair in zebrafish.

422 To date, cellular growth across the lesion has served as a primary readout of cellular
423 regeneration in zebrafish. Glial bridging and axon tracing assays were performed to evaluate the
424 extents of glial and axonal regeneration in iNeuron gene crispants. By Gfap immunostaining, the
425 cross-sectional area of glial bridges was 65% reduced in *atf3* cripants at 4 wpi, but was unaffected
426 in *vamp4* and *syt11a;syt11b* crispants compared to controls (Fig. 8D-E). At this time point,
427 anterograde axon tracing using Biocytin showed comparable axon regrowth from hindbrain
428 neurons into the proximal and distal SC sections between *vamp4*, *syt11a;syt11b* and control
429 animals (Fig. 8F-G). Consistent with their defective glial bridging, axon regrowth into the proximal
430 and distal sections of caudal SC tissues was markedly impaired in *atf3* cripants. Thus, *vamp4* and
431 *syt11a/b* are required for functional SC repair but dispensable for cellular regeneration across the
432 lesion. These studies showed iNeurons play essential regeneration-independent plasticity-based
433 roles after SCI, and indicated vesicular trafficking is required for the recovery of local neuronal
434 circuitry during innate SC repair.

DISCUSSION

435 This study presents a single-cell atlas of innate SC repair in adult zebrafish, uncovers neurons as
436 potent signaling hubs after SCI, identifies cooperative modes of regeneration- and plasticity-
437 based neuronal repair, and shows essential roles for vesicular trafficking in spontaneous neuronal
438 plasticity.

439 The single-cell dataset generated in this study offers a comprehensive resource to determine
440 regenerative cell identities and mechanisms in highly regenerative vertebrates. The use of
441 snRNA-seq is ideal to profile the majority of spinal cell types in zebrafish. Single-cell RNA
442 sequencing is inherently biased against larger cell types such as neurons and astrocytes (Lake
443 et al., 2017; Bakken et al., 2018; Wu et al., 2019). snRNA-seq reduces the challenges of cell
444 dissociation, retrieving large numbers of neurons and glia. While dissection- and dissociation-
445 induced gene expression changes in control samples present a longstanding difficulty for tissue

446 regeneration studies, our protocol minimizes background activation of injury-induced genes by
447 flash-freezing SC tissues from individual animals during tissue collection. Finally, large numbers
448 of nuclei were obtained by pooling frozen SC tissues, minimizing confounding problems
449 associated with snRNA-seq and allowing us to identify small cell populations (Lacar et al., 2016;
450 Lake et al., 2017; van den Brink et al., 2017; Bakken et al., 2018; Ding et al., 2020). Overall, this
451 dataset faithfully represents the proportions and dynamics of major cell populations during
452 zebrafish SC regeneration.

453 Candidate approaches have unveiled central roles for several signaling pathways during SC
454 regeneration (Reimer et al., 2009; Dias et al., 2012; Goldshmit et al., 2012; Zhang et al., 2018;
455 Cavone et al., 2021). Yet, an integrated assessment of regenerative signaling pathways and
456 global assessment of cell-cell interactions were missing. Using CellChat analysis, our single-cell
457 dataset identified a myriad of cell-specific and injury-induced signaling pathways (Jin et al., 2021).
458 Notably, comprehensive assessment of cell-cell signaling networks uncovered neurons as potent
459 sources of signaling in homeostatic and lesioned SC tissues. Injury-induced neuronal signaling
460 pathways include promoters of axon regrowth, survival, and migration such as L1CAM and CNTN
461 (Walsh and Doherty, 1996; Zhang et al., 2008; Zhu et al., 2015). Equally enriched in neurons
462 were repellent guidance molecules such as TENASCIN-R, SEMA3B and SEMA3C, enabling
463 proper axon guidance and synapse targeting (Cohen et al., 2001; Becker et al., 2004; Falk et al.,
464 2005; Ferrario et al., 2012). Further studies of injury-induced signaling pathways will shed light
465 into signaling pathways that direct regeneration- or plasticity-driven SC repair.

466 SC tissues in adult zebrafish retain potent progenitor cells with radial glial features and
467 established contribution to neurogenesis after SCI (Reimer et al., 2008; Briona et al., 2015;
468 Saraswathy et al., 2022). SC regeneration is marked by early imbalance and late restoration of
469 baseline E/I activity. Our data support a model in which excitatory neurons expand and repopulate
470 regenerate SC tissues, while slower and continued neurogenesis of inhibitory neurons underlie
471 the recovery of E/I balance at 6 wpi. These findings are consistent with published studies using a
472 two-cut SCI model in adult zebrafish (Huang et al., 2021), and with the observation that
473 *gad1b*:GFP and *vglut2a*:RFP expression domains are mutually exclusive in our SC sections.
474 Genetic lineage tracing showed excitatory to inhibitory neurotransmitter switching has adverse
475 effects on functional recovery after adult mouse SCI (Bertels et al., 2022). In zebrafish, fast motor
476 neurons were shown to upregulate glutamate expression after injury or exercise (Bertuzzi et al.,
477 2018). Although we cannot rule out similar mechanisms taking place in zebrafish, we found that

478 a steady increase in the profiles of newly generated excitatory and inhibitory neurons account for
479 the recovery of E/I balance after SCI. We propose that in depth molecular evaluation of spinal
480 progenitors is needed to better understand the potency and neurogenic capacities of neuronal
481 progenitors during SC regeneration.

482 While zebrafish is an established model of neuron regeneration, our study establishes
483 zebrafish as a renewed model to understand and manipulate fundamental mechanisms of
484 plasticity-based neuronal repair. Neurogenesis-based neural repair is thought to be unattainable
485 in mammals. Instead, the mammalian SCI field has directed its efforts to develop plasticity-based
486 repair strategies. We propose that pre-existing zebrafish neurons upregulate an iNeuron
487 transcriptional signature that includes regeneration associated genes, and that iNeurons elicit
488 spontaneous plasticity during early stages of SC repair. The emergence of iNeurons after SCI is
489 consistent with a recently identified population of embryonically derived dormant neurons that
490 immediately respond to SCI in larval and adult zebrafish (Vandestadt et al., 2021). Similarity to
491 the dormant precursor neurons reported by Vandestadt *et al.,* more than 90% of iNeurons are
492 non-regenerating. At 1 wpi, iNeuron signaling accounts for the majority of total neuronal signaling,
493 eliciting particularly strong interactions with OPCs. Intriguingly, cross-species transcriptomics
494 highlighted transcriptional similarities between iNeurons and a rare population of spontaneously
495 plastic spinocerebellar neurons (Matson et al., 2022). We propose that future zebrafish studies
496 will contribute insights and applications into mechanisms of plasticity-driven neural repair.

497 Unbiased characterization of the molecular players that direct iNeuron functions after SCI
498 showed multiple components of vesicular trafficking are required for functional SC repair in
499 zebrafish. Syt11a/b (synaptotagmin XI a/b) and Vamp4 (vesicle-associate membrane protein 4)
500 are vesicle-associated proteins that play different roles in neuronal synapses. Syt11 is a non-
501 canonical SNARE that inhibits spontaneous neurotransmission and bulk endocytosis, whereas
502 Vamp4 promotes Calcium-dependent excitatory neurotransmission release and bulk endocytosis
503 (Nicholson-Fish et al., 2015; Wang et al., 2016; Shimojo et al., 2019; Lin et al., 2020; Bakr et al.,
504 2021; Li et al., 2021). Our CRISPR/Cas9 studies showed *syt11a/b* and *vamp4* are required for
505 the recovery of swim function after SCI in zebrafish. These findings are consistent with recent
506 mammalian studies showing that inhibition of the presynaptic release machinery is important for
507 axon regrowth (Hilton et al., 2022), and that *Syt11* knockout in excitatory forebrain neurons
508 impairs synaptic plasticity and memory (Shimojo et al., 2019). Our data reveals vesicular
509 trafficking is an essential mechanism that underlies spontaneous plasticity and rapid neurite

510 outgrowth in iNeurons. We propose that zebrafish provide a valuable model to investigate the
511 origin of iNeurons, elucidate the role of vesicular trafficking in spontaneous plasticity, and identify
512 new manipulations to promote plasticity after SCI.

ACKNOWLEDGMENTS

We thank S. Ackerman, V. Cavalli and A. Johnson for discussion and the Washington University Zebrafish Shared Resource for animal care. This research was supported by grants from the NIH (R01 NS113915 to M.H.M.) and a Postdoctoral Fellow Seed of Independence Grant from the Department of Developmental Biology at Washington University School of Medicine (to V.M.S.).

MATERIAL AND METHODS

517 **Zebrafish**

518 Adult zebrafish of the Ekkwill, Tubingen and AB strains were maintained at the Washington
519 University Zebrafish Core Facility. All animal experiments were performed in compliance with
520 institutional animal protocols. Size matched (~2 cm) male and female animals of ~4 months of
521 age were used. SC transection surgeries and regeneration analyses were performed in a blinded
522 manner. For all experiments, 2 to 4 independent experimental replicates were performed using
523 different clutches of animals. Within each experiment, experimental fish and control siblings of
524 similar size and equal sex distribution were used. Transected animals from control and
525 experimental groups were housed in equal numbers (4-7 fish) in 1.1-liter tanks. The following
526 previously published zebrafish trains were used: Tg(*vglut2a*:RFP) and Tg(*gad1b*:GFP) (Satou et
527 al., 2013).

528 **Spinal cord transection**

529 Complete SC transections were performed as previously described (Mokalled et al., 2016).
530 Briefly, zebrafish were anaesthetized in 0.2 g/L of MS-222 buffered to pH 7.0. Fine scissors were
531 used to make a small incision that transects the SC 4 mm caudal to the brainstem region.
532 Complete transection of the SC was visually confirmed at the time of surgery. Injured animals
533 were also assessed at 2 or 3 dpi to confirm loss of swim capacity post-surgery.

534 **Isolation of spinal cord nuclei from adult zebrafish**

535 For nuclear isolation, a previously described method to isolate nuclei from mouse SC tissues was
536 adapted to zebrafish SCs (Matson et al., 2018). Three mm SC tissue, flanking the lesion site were
537 collected from 50 adult zebrafish at timepoints 1, 3 and 6 wpi. Corresponding segments of 3 mm
538 SC tissue were collected from uninjured control animals. For tissue lysis, the detergent
539 mechanical lysis protocol described by Matson et al. was performed. SC tissues were
540 homogenized at low setting for 15 seconds. Density gradient separation using sucrose solution
541 was used to sediment the nuclei from the supernatant. Final nuclear lysates were resuspended
542 using 100 µl of resuspension solution (1x PBS + 2% BSA + 0.2U/µl RNase inhibitor - New England
543 Biolabs, Cat#: M0314S). Hoechst staining was performed to assess the quality of isolated nuclei
544 based on their shape. Samples in which more than 70% of the nuclei were scored as 'healthy'
545 and submitted for single nuclear RNA sequencing.

546 **Single nuclear RNA sequencing**

547 For snRNA-seq, 30 µl of resuspension solution containing isolated nuclei at a concentration of
548 ~1000 nuclei/µl was submitted to Genome Technology Access Center at McDonnel Genome
549 Institute of Washington University. Two biological replicates of each timepoints at 0, 1, 3 and 6
550 wpi were used. cDNA was prepared after the GEM generation and barcoding, followed by the
551 GEM-RT reaction and bead cleanup steps. cDNA was amplified for 11-13 cycles then purified
552 using SPRIselect beads. Purified cDNA samples were then run on a Bioanalyzer to determine the
553 cDNA concentration. GEX libraries were prepared as recommended by the 10x Genomics
554 Chromium Single Cell 3' Reagent Kits User Guide (v3.1 Chemistry Dual Index) with appropriate
555 modifications to the PCR cycles based on the calculated cDNA concentration. For sample
556 preparation on the 10x Genomics platform, the Chromium Next GEM Single Cell 3' Kit v3.1, 16
557 rxns (PN-1000268), Chromium Next GEM Chip G Single Cell Kit, 48 rxns (PN-1000120), and Dual
558 Index Kit TT Set A, 96 rxns (PN-1000215) were used. The concentration of each library was
559 accurately determined through qPCR utilizing the KAPA library Quantification Kit according to the
560 manufacturer's protocol (KAPA Biosystems/Roche) to produce cluster counts appropriate for the
561 Illumina NovaSeq6000 instrument. Normalized libraries were sequenced on a NovaSeq6000 S4
562 Flow Cell using the XP workflow and a 50x10x16x150 sequencing recipe according to
563 manufacturer protocol. A median sequencing depth of 50,000 reads/cell was targeted for each
564 Gene Expression Library.

565 **Aligning snRNA-seq reads**

566 After sequencing, the Illumina output was processed using the CellRanger (v6.0.0) recommended
567 pipeline to generate gene-barcode count matrices. A custom reference genome was made with
568 the "cellranger mkref" command, using the fasta file of zebrafish reference genome GRCz11
569 constructed from the Ensemble genome build (https://useast.ensembl.org/Danio_rerio/Info/Index)
570 and the sorted Gene Transfer Format file (v4.3.2) from the improved zebrafish transcriptome
571 annotation (Lawson et al., 2020). Base call files for each sample from Illumina were demultiplexed
572 into FASTQ reads. Then, the "cellranger count" pipeline was used to align sequencing reads in
573 FASTQ files to the custom reference genome. Both exon and intron sequences were included
574 during the alignment. The filtered gene-barcode count matrices generated by "cellranger count"
575 was used for downstream analysis.

576 **Integrated analysis of snRNA-seq dataset**

577 All the datasets were integrated and analyzed using Seurat (v4.1.1) package with R (v4.2.1) (R
578 Core Team, 2018; Stuart et al., 2019). Each sample count matrix was filtered for genes that were

expressed in at least 3 cells and cells expressing at least 200 genes, followed by cell quality assessment using commonly used QC matrixes (Ilicic et al., 2016). Cells having a unique number of genes between 200 to 4000 and a mitochondrial gene percentage <5 were used for downstream processing. Each dataset was independently normalized and scaled using the "SCTransform" function, which is an improved method for normalization, that performs a variance-stabilizing transformation using negative binomial regression (Hafemeister and Satija, 2019). Standard integration workflow of Seurat was used to identify shared sources of variation across experiments as well as mutual nearest neighbors (Butler et al., 2018; Haghverdi et al., 2018). Integration features were selected based on the top 4000 highly variable features using "SelectIntegrationFeatures" function (nfeatures = 4000), which was used as input for the "anchor.features" argument of the "FindIntegrationAnchors" function. PCA analysis was performed on the 4000 variable features and the top 50 principal components selected based on the elbow plot heuristic, which measures the contribution of variation in each component. These 50 principal components were used in "FindNeighbors" and "FindClusters" functions to perform graph-based clustering on a shared nearest neighbor graph (Levine et al., 2015; Xu and Su, 2015). Louvain algorithm was used for modularity optimization in clustering the cells using "FindClusters" function. The resolution parameter (res = 0.5) that determines the granularity of the clustering was selected by visually inspecting clusters with resolutions ranging 0.1 - 2.0 as well as clustree graphs (Zappia and Oshlack, 2018). Uniform Manifold Approximation and Reduction (UMAP) was used for non-linear dimensional reduction of the first 50 principal components and visualize the data using "RunUMAP" function (Becht et al., 2018). Data was graphed using different plot functions, such as "DimPlot", "VlnPlot", "FeaturePlot", "Dotplot" and "DoHeatmap", to view the cell cluster identity and marker gene expression. Cell proportion data was extracted using "table" and "prop.table" functions. Differential gene expression for individual cluster was identified using Wilcoxon rank sum test in the "FindAllMarkers" function. Marker genes detected in at least 25% of the clustered cells and with a logFC threshold of 0.25 were selected. Only positive markers were reported.

Subset analysis of neuron clusters

The neuron cell clusters identified from the complete dataset were subclustered using the "subset" function for subcluster analysis. The subset was again normalized and scaled using "SCTransform" function with glmGamPoi method (Ahlmann-Eltze and Huber, 2021). Fifty principal components were used, and the resolution parameter was set to 0.5. Further downstream analysis was done as described above for the integrated analysis. The top DE markers generated

612 for each neuron subcluster using “FindAllMarkers” function is given in the supplementary table
613 S3.

614 **Cluster identification using differentially expressed markers.**
615 A “CNS markers” database of previously published markers of the different cell types that
616 comprise the vertebrate brain and/or SC tissues was compiled (Guillemot, 2007; Zhang et al.,
617 2014; Lu et al., 2015; Hernandez-Miranda et al., 2017; Tang et al., 2017; Haring et al., 2018;
618 Hayashi et al., 2018; Rosenberg et al., 2018; Sathyamurthy et al., 2018; Zeisel et al., 2018; Baek
619 et al., 2019; Rougeot et al., 2019; Tambalo et al., 2020; Cavone et al., 2021; Milich et al., 2021;
620 Yadav et al., 2023). For each cell cluster, every marker gene identified as a top differentially
621 expressed (DE) marker of that cluster was cross-referenced with our compiled “CNS markers”
622 database. For every matching marker gene, one point was given to the respective cluster under
623 the column name with the matching cell identity. Iteration over every marker gene was performed
624 to generate a scoring matrix with varying points for each cluster against the different cell identities
625 compiled in the “CNS markers” database (Table S2, scoring). Then, “phyper” function in R was
626 used to calculate binomial probabilities using hypergeometric distribution for the total score
627 obtained by each cluster against each cell identity in the database (Table S2, Binomial
628 probability). Then, -log10 of probability values are obtained for plotting the heatmap (Table S2, -
629 log10P). The resulting values were scaled to 0-100 and plotted as a heatmap using GraphPad
630 prism. Each cluster was given an identity based on the maximum -log10 P score obtained in the
631 heatmap. The top DE markers of clusters with ambiguous scores (e.g., 20, 24, 35 and 39) are
632 manually searched in the literature for deciding cluster identity. “RenameIdents” function was
633 used to assign identity to each cluster. For confirmation of the assigned cluster identity,
634 enrichment of classical markers of respective cell types were tested using Dot plot.
635 (https://github.com/vishnums007/Zebrafish-SCI-atlas/blob/main/s7_marker_comparison_v3.R)

636 **Filtering differentially expressed markers for candidate gene selection.**
637 To identify candidate genes that are uniquely expressed in N22 iNeurons, top DE markers were
638 cross-checked and filtered against the top DE markers of all the other neuron subclusters.
639 Enrichment and percent expression of these unique genes were then confirmed using Dot plots.
640 Genes that were enriched or expressed in other neuronal or non-neuronal subclusters, in addition
641 to their expression in iNeurons, were omitted. Genes that are exclusively enriched in iNeurons
642 were selected for generating crispants.

643 **Cell-cell interaction assay**

644 The R package CellChat (v1.4.0) was used to evaluate regenerative cell-cell interactions after
645 SCI (Jin et al., 2021). CellChat models the probability of cell-cell communication by integrating
646 our gene expression data with a database (CellChatDB) of known interaction between signaling
647 ligands, receptors, and their cofactors. CellChatDB is a manually curated from literature-
648 supported ligand-receptor interactions in human and mouse, only. Therefore, we converted the
649 normalized RNA data matrix of our zebrafish dataset at each timepoint into human orthologues
650 using Ensemble biomaRT package (Durinck et al., 2009). The following rules were applied while
651 converting the data matrix: 1) one-to-one orthologue mapping was performed whenever possible,
652 2) For genes with one to several human orthologues, the corresponding zebrafish RNA data value
653 was copied to every mapped gene in humans, 3) RNA data values were eliminated for zebrafish
654 genes that did not have any human orthologue, 4) RNA data values of paralogous zebrafish genes
655 were added and the cumulative data value was assigned to the human orthologue
656 (https://github.com/vishnums007/Zebrafish-SCI-
657 atlas/blob/main/Sparse_matrix_homologe_converter_082322.R) . The converted RNA data was
658 used then to create CellChat object using "createCellChat" function, followed by the
659 recommended preprocessing functions with default parameters for the analysis of individual
660 datasets. CellChatDB.human was used as the database for inferring cell-cell communication. All
661 categories of ligand-receptor interactions in the database were used in the analysis.
662 Communications involving less than 10 cells were excluded. Function
663 "netAnalysis_computeCentrality" was used to calculate network centrality scores at each
664 timepoint. Functions such as "netVisual_circle", "netAnalysis_contribution",
665 "netVisual_aggregate", "netVisual_bubble" and "netAnalysis_signalingRole_heatmap" were used
666 to generate different plots used in this paper.

667 **Trajectory inference analysis**

668 Pseudotime analysis was performed using CellRank (v1.5.1) package in Python (v3.8.10)
669 (Rossum and Drake, 2009; Lange et al., 2022). Before analysis, the Seurat object was converted
670 to an AnnData in a two-step process using the R package SeuratDisk (v0.9020). First, the Seurat
671 object was saved as an h5Seurat file and then, converted it to an AnnData file to use as an input
672 for pseudotime analysis using CellRank. Basic pre-processing of the AnnData file was performed
673 with default recommended settings using the scvelo (v0.2.4) and scanpy (v1.9.1) packages.
674 Genes expressed in at least 10 cells were included and 30 principal components and neighbors
675 were used for preprocessing of the data. CytoTRACEkernel was used for pseudotime

676 computation and direct KNN graph-edges to point into the direction of increasing differentiation
677 status (Gulati et al., 2020). The transition matrix was calculated by setting the threshold_scheme
678 parameter to “soft” to reconstruct cellular trajectories using VIA algorithm (Stassen et al., 2021).
679 This transition matrix was projected onto a UMAP plot to obtain a velocity graph.

680 **Gene ontology**

681 Gene ontology analysis was performed using Metascape (Zhou et al., 2019). Input and analysis
682 species were set as D. rerio. Express analysis was performed for gene ontology. Metascape
683 identified all statistically enriched terms (including GO biological processes, Reactome gene set
684 and KEGG pathway), and calculated accumulative hypergeometric p-values and enrichment
685 factors. Significant terms were hierarchically clustered into a tree based on Kappa-statistical
686 similarities among their gene memberships. A kappa score of 0.3 was applied to cast the tree into
687 term clusters. The most enriched term in each cluster was chosen as the representative term.

688 **Cross-species comparison of DE markers**

689 To compare the DE markers of iNeuron and RAG clusters, top markers identified using Wilcoxon
690 rank sum test in the “FindAllMarkers” function were selected for iNeurons (clusters N18 and N22
691 in the zebrafish dataset) and for the RAG cluster (identified using markers used in *Matson et al.,*
692 *2022* in the mouse dataset GSE172167). Marker genes detected in >25% of the clustered cells
693 and with a logFC threshold of 0.25 were selected. Only positive markers were used. R package
694 *ggvenn* (v0.1.9) was used to plot the venn diagram to compare the top markers of the 3 clusters.
695 Metascape (Zhou et al., 2019) analysis using “multiple gene list” was used to generate the Gene
696 Ontology comparison between zebrafish and mouse clusters.

697 **Cross-species transcriptomics**

698 Neuron subsets from zebrafish (Fig. 1) and mouse (GSE172167) datasets were used for cross-
699 species data integration. Prior to integration, a custom made R script (as previously mentioned
700 during CellChat analysis) was used to convert the RNA count matrix of zebrafish neurons into
701 their mouse orthologues using the Ensemble biomaRT package (Durinck et al., 2009). The
702 following rules were applied while converting the data matrix: 1) one-to-one orthologue mapping
703 was performed when possible, 2) For genes with one to several mouse orthologues, the
704 corresponding zebrafish RNA data value was copied to every mapped gene in mouse, 3) RNA
705 data values were eliminated for zebrafish genes that did not have any mouse orthologue, 4) RNA
706 data values of paralogous zebrafish genes were added and the cumulative data value was

707 assigned to the mouse orthologue. Following gene conversion, the zebrafish and mouse datasets
708 were integrated using Seurat package with 6000 highly variable features. Resolution 1.1 was
709 used for cluster analysis of the integrated dataset.

710 **Histology**

711 Sixteen µm cross cryosections of paraformaldehyde fixed SC tissues were used. Tissue sections
712 were imaged using a Zeiss LSM 800 confocal microscope for immunofluorescence and
713 hybridization chain reaction (HCR) RNA *in situ* hybridization.

714 The HCR RNA *in situ* hybridization protocol was adapted from Molecular Instruments
715 (https://www.molecularinstruments.com/hcr-ihc-protocols) (Choi et al., 2018). Briefly, tissue
716 sections were hydrated in PBS, dehydrated stepwise into 100% ethanol, then rehydrated stepwise
717 into PBT (0.1% Tween-20 in PBS). Sections were pre-treated either with 0.2% TritonX-100 in
718 PBS for 5 minutes or boiled in Citrate Buffer (10mM Citric Acid, 0.05% Tween-20, pH 6.0) for 10
719 minutes. For blocking, sections were incubated in Hybridization buffer (Molecular Instruments) for
720 1 hr at 37°C. For hybridization, sections were incubated in pre-warmed DNA probe sets diluted to
721 0.0015 pmol/uL in Hybridization buffer for 48 hrs at 37°C. Washes were then performed with Wash
722 Buffer (Molecular Instruments) at 37°C followed by 5x SSCT (3M NaCl, 0.3 M Sodium Citrate,
723 0.1% Tween-20, pH 7.0). For signal amplification, sections were incubated in Amplification buffer
724 (Molecular Instruments) for 1 hr at room temperature. Prior to amplification, h1 and h2 hairpins
725 were snap-cooled in individual tubes by heating to 95°C and allowing tubes to return to ambient
726 temperature slowly. For amplification, h1 and h2 snap-cooled hairpins were mixed together and
727 diluted 1:50 in Amplification buffer. Amplification proceeded overnight at room temperature in the
728 dark. Samples were then washed thoroughly in 5x SSCT, 5x SSC, and PBT at room temperature
729 before proceeding to immunohistochemistry. HCR RNA probes used in this study (*syt11a, syt11b,*
730 and *vamp4*) were designed using a python script. Probe sets were ordered as 50 pmol opools
731 from IDT. Oligo sequences for each probe set are provided in Table S4.

732 For immunohistochemistry, tissue sections were hydrated in PBT then treated with blocking agent
733 (5% goat serum in PBT) for 1 hr at room temperature. For nuclear antigens, sections were treated
734 with 0.2% TritonX-100 in PBT for 5 minutes and washed thoroughly in PBT prior to the blocking
735 step. Sections were incubated overnight at 4°C with respective primary antibodies diluted in
736 blocking agent, then washed in PBT, and treated for 1 hour in secondary antibodies diluted in
737 blocking agent at room temperature. For EdU staining, sections are incubated with freshly

738 prepared EdU staining solution (100mM Tris at pH 8.5 - SIGMA T6066, 1 mM $CuSO_4$ – SIGMA
739 C1297, 200 µM Fluorescent azide – Thermo Fischer Scientific and 100 mM Ascorbic Acid -
740 SIGMA A5960) for 30 minutes in the dark at room temperature (Salic and Mitchison, 2008).
741 Following washes, sections were incubated in 1 µg/mL of Hoechst (Thermo Scientific, H3570) for
742 3 minutes, washed in PBT and mounted in Fluoromount-G mounting media (SouthernBiotech,
743 0100-01). Primary antibodies used in this study were chicken anti-GFP (AVES, 1020, 1:1000),
744 rabbit anti-dsRed (Clontech, 632496, 1:250), mouse anti-HuC/D (Invitrogen, A21271, 1:500).
745 Secondary antibodies (Invitrogen, 1:250) used in this study were Alexa Flour 488, Alexa Flour
746 594, and Alexa Flour 647 goat anti-rabbit or goat anti-mouse antibodies.

747 **CRISPR/Cas9 mutagenesis**

748 CRISPR/Cas9 design, mutagenesis and screening was performed as previously described (Klatt
749 Shaw and Mokalled, 2021). Briefly, crRNA guide RNA sequences were selected using
750 CHOPCHOP (https://chopchop.cbu.uib.no/). Only sequences with no off-target sites with three or
751 fewer mismatches elsewhere in the genome were selected. To maximize the effect of small indels,
752 target sites were chosen that lie within essential domains (Table S5). Alt-R tracrRNA and crRNA
753 gRNAs (IDT, Cat# 1072534) were reconstituted using manufacturer's specifications as 100 µM
754 stocks, then annealed at a final concentration of 50 µM. Alt-R S.p. Cas9 nuclease V3 (IDT, Cat#
755 1081059) was diluted in Cas9 dilution buffer (1 M HEPES at pH 7.5, 2 M KCl) to a working
756 concentration of 25 µM. Annealed dgRNA duplexes were diluted 1:1 in duplex buffer (IDT, Cat#
757 11-05-01-03) to a working concentration of 25 µM. Equal volumes of dgRNA were added to Cas9
758 protein and incubated at 37°C for 5 minutes. For dual targeting of *syt11a* and *syt11b*, Cas9 protein
759 was added in equal molar amounts to the total concentration of dgRNA. Tubingen wild-type
760 embryos were injected with 1 nL of CRISPR/Cas9 solution at the one-cell stage and grown to
761 adulthood for genotyping, SC surgeries and functional analysis. The full sequence for each guide
762 RNAs is provided in Table S5.

763 **Genotyping by capillary electrophoresis**

764 Capillary electrophoresis was used to calculate the indel frequency for each CRISPR/Cas9 target
765 site. For DNA extraction, whole 4 dpf larvae or ~3 mm of excised adult tail fins were added to 20
766 µL (larvae) or 50 µL (adult fin) of fin lysis buffer (10 mM Tris at pH 7.0, 50 mM KCl, 1 mM EDTA
767 at pH 8.0, 0.3% Tween-20, freshly added Proteinase K at 200 µg/ml). DNA samples were
768 incubated at 55°C for 60 minutes and then, followed by a 15-minute incubation at 95°C. 150-250
769 bp PCR products were generated using NEB Taq Polymerase (Cat# M0273) with gene-specific

770 primers (Table S5) in a volume of 10 μL in Pryme PCR semi-skirted PCR plates (MidSci, Cat#
771 AVRT1). Samples were diluted to 24 μL in TE dilution buffer (Agilent, DNF-495-0060) and loaded
772 into the 5200 Fragment Analyzer System (Agilent, Cat# M5310AA). Capillary electrophoresis was
773 carried out using the Agilent Fragment Analyzer Qualitative DNA Kit (Cat# DNF-905-K1000)
774 according to the manufacturer's specifications.

775 To calculate indel frequency, 2 wild-type control siblings were PCR amplified. The size of wild-
776 type products was determined using these control samples. PCR products with peaks within 1 bp
777 of control amplicon size were termed wild types (non-indel). Indel frequency was calculated by
778 dividing the signal intensity of total non-indel peaks by the cumulative intensity of all peaks in each
779 sample. Because of significant noise due to primers (<100 bp) and non-specific products (>300
780 bp) in wild-type samples, only signals between 100 and 300 bp were used to calculate indel
781 frequency.

782 **Swim endurance assay**

783 Swim endurance assays were performed as previously described (Burris et al., 2021). Zebrafish
784 were exercised in groups of 8-15 in a 5 L swim tunnel device (Loligo, Cat# SW100605L,
785 120V/60Hz). After 5 minutes of acclimation (with no flow) inside the enclosed tunnel, fish were
786 swum at 9 cm/s and 10 cm/s for 5 minutes each to evaluate their swimming capability at bare
787 minimum velocity. Water current velocity was then increased every two minutes and fish swam
788 against the current until they reached exhaustion. Exhausted animals were removed from the
789 chamber without disturbing the remaining fish. Swim time at exhaustion was recorded for each
790 fish. Fish that were exhausted before the first 15 minutes were considered poorly recovered.
791 Percent recovery was calculated by dividing the number of fish that swam more than 15 minutes
792 to the total number of fish present in the group.

793 **Swim behavior assay**

794 Swim behavior assays were performed as previously described (Burris et al., 2021). Zebrafish
795 were divided into groups of 5 in a 5 L swim tunnel device (Loligo, Cat# SW100605L, 120V/60Hz).
796 Each group was allowed to swim for a total of 15 min under zero to low current velocities (5 min
797 at 0 cm/s, 5 min at 10 cm/s, and 5 min at 15 cm/s). The entire swim session was recorded using
798 high-speed camera (iDS, USB 3.0 color video camera) with following settings: aspect ratio, 1:4;
799 pixel clock, 344; frame rate, 70 frames/s; exposure time: 0.29; aperture, 1.4 to 2; maximum
800 frames; 63,000. Movies were converted to 20 frames/s and analyzed using a customized Fiji

801 macro (https://github.com/vishnums007/Zebrafish-SCI-
802 atlas/blob/main/Swim%20behavior_Tracking_v2.ijm). For each frame, animals/objects >1500 px2
803 were identified, and the XY coordinates were derived for each animal/object. Each frame was
804 independently analyzed, and animal/object tracking was completed using a customized R Studio
805 script(https://github.com/vishnums007/Zebrafish-SCI-
806 atlas/blob/main/SwimBehavior_processing%20and%20quantification_v7.R). The script aligned
807 coordinates, calculated swim metrics considering three separate frame windows (Frames 0-6000
808 at 0 cm/s; frames 6001-12000 at 10 cm/s, and frames 12001-18001 at 20 cm/s). Distance swam
809 was analyzed at 0, 10, and at 15 cm/s.

810 **Axon tracing assay**

811 Anterograde axon tracing was performed on adult zebrafish at 28 dpi as previously described
812 (Mokalled et al., 2016). Fish were anaesthetized using MS-222 and fine scissors were used to
813 transect the cord 4 mm rostral to the lesion site. Biocytin-soaked Gelfoam Gelatin Sponge was
814 applied at the new injury site (Gelfoam, Pfizer, cat# 09-0315-08; Biocytin, saturated solution,
815 Sigma, Cat# B4261). Fish were euthanized 3 hours post-treatment and Biocytin was histologically
816 detected using Alexa Fluor 594-conjugated Streptavidin (Thermo Fisher, cat# S-11227). Biocytin-
817 labeled axons were quantified using the "threshold" and "particle analysis" tools in the Fiji
818 software. Four sections per fish at 0.5 (proximal) and 2 (distal) mm caudal to the lesion core, and
819 2 sections 1 mm rostral to the lesion, were analyzed. Axon growth was normalized to the efficiency
820 of Biocytin labeling rostral to the lesion for each fish. The axon growth index was then normalized
821 to the control group for each experiment.

822 **Glial bridging assay**

823 Gfap immunohistochemistry was performed on serial sections. The cross-sectional area of the
824 glial bridge and the area of the intact SC rostral to the lesion were measured using ImageJ
825 software. Bridging was calculated as a ratio of these measurements.

826 **Quantifications**

827 *Cell counting.* Cell counting were performed using a customized Fiji script (adapting ITCN plugin:
828 Image based Tool for counting nuclei- https://imagej.nih.gov/ij/plugins/itcn.html,
829 https://github.com/vishnums007/Zebrafish-SCI-atlas/blob/main/Cell_Counter_v1-5_vms.ijm).
830 Orthogonal projections of individual image stacks were generated using Zen software. A
831 customized Fiji script incorporated user-defined inputs to define channels (including Hoechst) and

832 to outline SC perimeters. To quantify nuclei, the following parameters were set in ITCN counter:
833 width – 15; minimal distance – 7.5; threshold – 0.4. Once nuclei were identified, user-defined
834 thresholds of individual cell markers were used to mask the image and identify nuclei located
835 inside the masked regions. X/Y coordinates were extracted for each nucleus for cell counting.
836 Raw counts and X/Y coordinates from Fiji were processed using a customized R script
837 (https://github.com/vishnums007/Zebrafish-SCI-
838 atlas/blob/main/Cell_Count_Processor_v1_vms.R). Markers that share nuclei with the same X/Y
839 coordinates were considered overlapping.

840 *Quantifying HCR in situ signal.* HCR *in situ* hybridization signals were quantified using custom
841 made Fiji script (https://github.com/vishnums007/Zebrafish-SCI-
842 atlas/blob/main/hcr_celltypespecific_analysis_v3.1_080222.ijm). Orthogonal projections of
843 individual image stacks were generated using the Zen software (Zeiss). ROIs around SC borders
844 were defined to exclude non-SC tissues and user-defined thresholds were set to create an
845 inverted mask. Background noise was either manually corrected or defined by thresholding a
846 dedicated, unstained background channel. Integrated density was quantified for fluorescence
847 signals inside the quantification mask using the "Analyze Particles" command. To calculate the
848 HCR *in situ* hybridization signal inside neurons, an inverted mask was created after thresholding
849 HuC/D^{+} neurons, then added to the final quantification mask. The fluorescence signals inside this
850 newly generated mask were considered neuron specific.

851 **Script availability**
852 All the scripts used in the study is available in GitHub (https://github.com/vishnums007/Zebrafish-
853 SCI-atlas).

854 **Data availability**
855 The snRNA-seq data for both all integrated cell types and neuron subset is available to explore
856 here: https://shinypath.wustl.edu/SCI_Atlas/

Figure 1

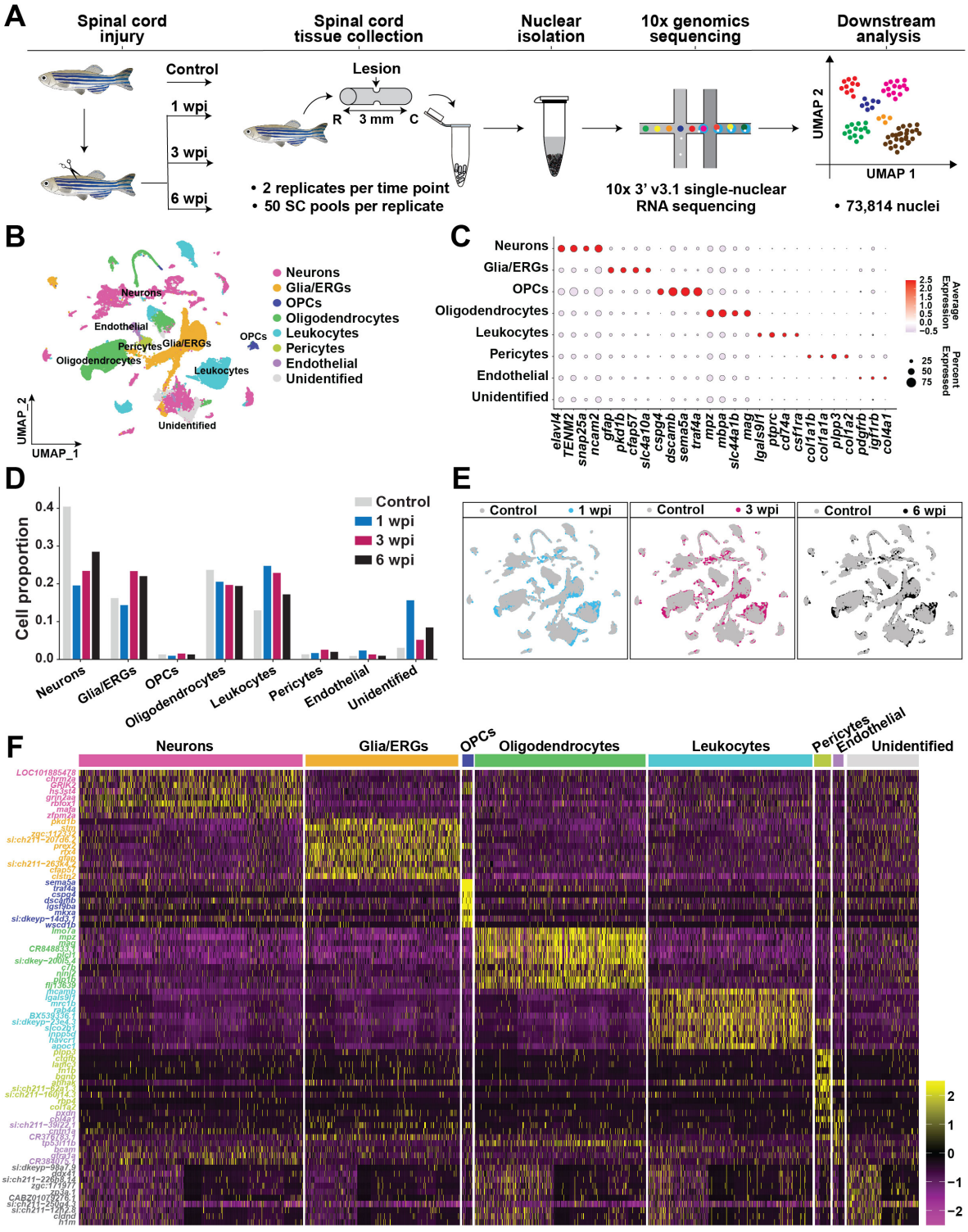
A
Spinal cord injury
Spinal cord tissue collection
Nuclear isolation
10x genomics sequencing
Downstream analysis
Control
1 wpi
3 wpi
6 wpi
Lesion
R
3 mm
C
• 2 replicates per time point
• 50 SC pools per replicate
10x 3' v3.1 single-nuclear RNA sequencing
UMAP 2
UMAP 1
• 73,814 nuclei
B
Neurons
Glia/ERGs
OPCs
Oligodendrocytes
Leukocytes
Pericytes
Endothelial
Unidentified
UMAP_2
UMAP_1
C
Average Expression
Percent Expressed
elavl4
TENM2
snap25a
ncam2
gfap
pkd1b
cfap57
slc4a10a
cspg4
dscamb
sema5a
traf4a
mpz
mbpa
slc44a1b
mag
lgals9l1
ptprc
cd74a
csf1ra
col1a1b
col1a1a
plpp3
col1a2
pdgfrb
igf1rb
col4a1
D
Cell proportion
Control
1 wpi
3 wpi
6 wpi
E
F

857 **Figure 1. Transcriptomic profiling of innate SC repair in adult zebrafish. (A)** Experimental
858 pipeline to generate a single-cell atlas of zebrafish cells after SCI. SC tissue collection, nuclear
859 isolation and single nuclear RNA-seq (snRNA-seq) were performed on wild-type fish were 1, 3
860 and 6 wpi. Uninjured SC nuclei were used as 0 wpi controls. 10x genomics sequencing with v3.1
861 chemistry was performed. Two biological replicates were used at each time point, and SC tissues
862 from 50 animals were pooled into a single biological replicate. **(B)** Merged UMAP representation
863 of the complete dataset. Two biological replicates, 4 time points and 73,814 cells were clustered
864 into major spinal cell populations including neurons, glia/ependymo-radial glial cells (glia/ERGs),
865 oligodendrocyte precursor cells (OPCs), and oligodendrocytes. **(C)** Marker gene expression in
866 the major cell types identified after SCI. Dot plot shows canonical marker genes are enriched in
867 their respective cell types identified. Dot colors and diameters represent average gene expression
868 and percent cells with at least one UMI detected per gene, respectively. **(D)** Distribution of major
869 cell types during SC regeneration. For each time point, cell proportions were to the total number
870 of cells present at that time point. **(E)** Overlapping UMAP plots highlight broad changes in cell
871 populations between 1, 3, or 6 wpi relative to uninjured controls. **(F)** Heatmap showing top 10
872 differentially expressed (DE) genes in the major cell populations identified by snRNA-seq. Yellow
873 and magenta colors represent highly enriched and low-expression genes, repectively.

Figure 2

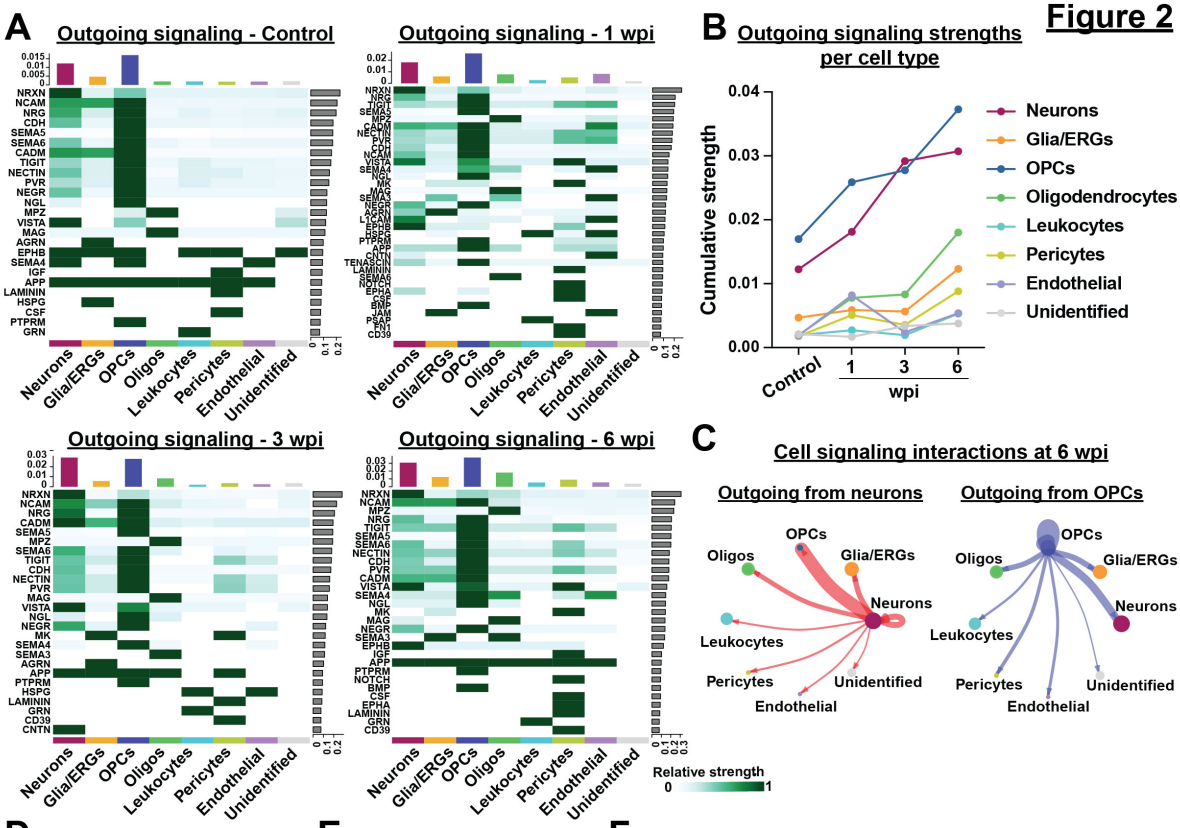

D Integrated outgoing signaling

Rank	Control	1 wpi	3 wpi	6 wpi
1	NRXN	NRXN	NRXN	NRXN
2	NCAM	NRG	NCAM	NCAM
3	NRG	TIGIT	NRG	MPZ
4	CDH	SEMA5	CADM	NRG
5	SEMA5	MPZ	SEMA5	TIGIT
6	SEMA6	CADM	MPZ	SEMA5
7	CADM	NECTIN	SEMA6	SEMA6
8	TIGIT	PVR	TIGIT	NECTIN
9	NECTIN	CDH	CDH	CDH
10	PVR	NCAM	NECTIN	PVR
11	NEGR	VISTA	PVR	CADM
12	NGL	SEMA4	MAG	VISTA
13	MPZ	NGL	VISTA	SEMA4
14	VISTA	MK	NGL	NGL
15	MAG	MAG	NEGR	MK
16	AGRN	SEMA3	MK	MAG
17	EPHB	NEGR	SEMA4	NEGR
18	SEMA4	AGRN	SEMA3	SEMA3
19	IGF	L1CAM	AGRN	EPHB
20	APP	EPHB	APP	IGF
21	LAMININ	HSPG	PTPRM	APP
22	HSPG	PTPRM	HSPG	PTPRM
23	CSF	APP	LAMININ	NOTCH
24	PTPRM	CNTN	GRN	BMP
25	GRN	TENASCIN	CD39	CSF
26		LAMININ	CNTN	EPHA
27		SEMA6		LAMININ
28		NOTCH		GRN
29		EPHA		CD39
30		CSF		
31		BMP		
32		JAM		
33		PSAP		
34		FN1		
35		CD39		

E Outgoing signaling from neurons

Rank	Control	1 wpi	3 wpi	6 wpi
1	NRXN	NRXN	NRXN	NRXN
2	NCAM	NRG	NCAM	NCAM
3	NRG	CADM	NRG	NRG
4	CDH	TIGIT	CADM	SEMA6
5	SEMA6	CDH	SEMA6	TIGIT
6	CADM	NECTIN	CDH	CDH
7	TIGIT	PVR	TIGIT	CADM
8	NECTIN	NCAM	NECTIN	MPZ
9	PVR	MPZ	PVR	NECTIN
10	VISTA	VISTA	VISTA	PVR
11	NEGR	SEMA5	MPZ	VISTA
12	NGL	EPHB	SEMA5	NEGR
13	SEMA5	NEGR	NEGR	EPHB
14	MAG	L1CAM	NGL	MAG
15	SEMA4	NGL	MAG	NGL
16	EPHB	AGRN	SEMA4	SEMA5
17	APP	SEMA4	APP	SEMA4
18		MAG	CNTN	APP
19		APP		
20		TENASCIN		
21		CNTN		
22		EPHA		

Enriched only at 1 wpi

Injury-induced genes

F

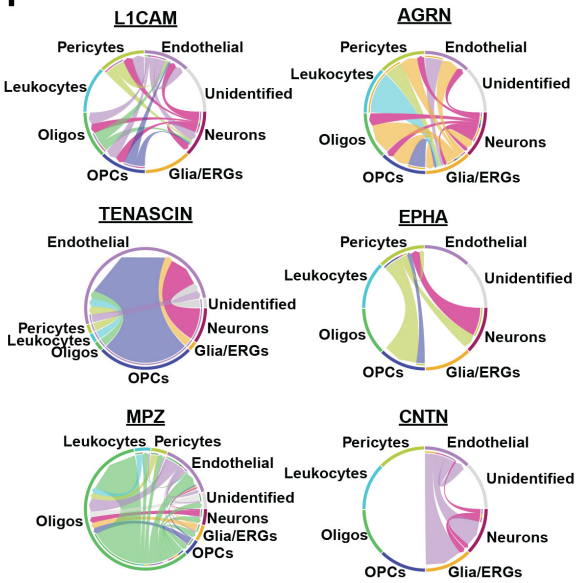

874 **Figure 2. Cell-cell interaction networks during SC regeneration. (A,B)** Relative strengths of
875 outgoing signaling pathways in major spinal cell populations at 0, 1, 3 and 6 wpi. Bar graphs at
876 the top of each heatmap show cumulative signaling strengths per cell population (A). Bar graphs
877 at the right of each heatmap show cumulative signaling strength per pathway (A). Panel B shows
878 elevated and dynamic cumulative strengths of signaling pathways outgoing from neurons and
879 OPCs. **(C)** Circle plots represent cell-cell interaction strengths of signaling pathways outgoing
880 from neurons and OPCs at 6 wpi. Arrow thickness is directly proportional to the cumulative
881 strengths of all predicted interactions between clusters. **(D,E)** Outgoing signaling pathways for the
882 complete dataset in D and for the neuron clusters in E. Pathways are ranked in the descending
883 order of their cumulative signal strengths. Pathways highlighted in magenta represent injury-
884 enriched signaling. Pathways highlighted in magenta and yellow represent signaling pathways
885 that are specifically enriched at 1 wpi. **(F)** Chord diagrams showing intercellular communication
886 of signaling pathways that are enriched in neurons after SCI. Arc diameters are proportional to
887 cumulative signaling strengths.

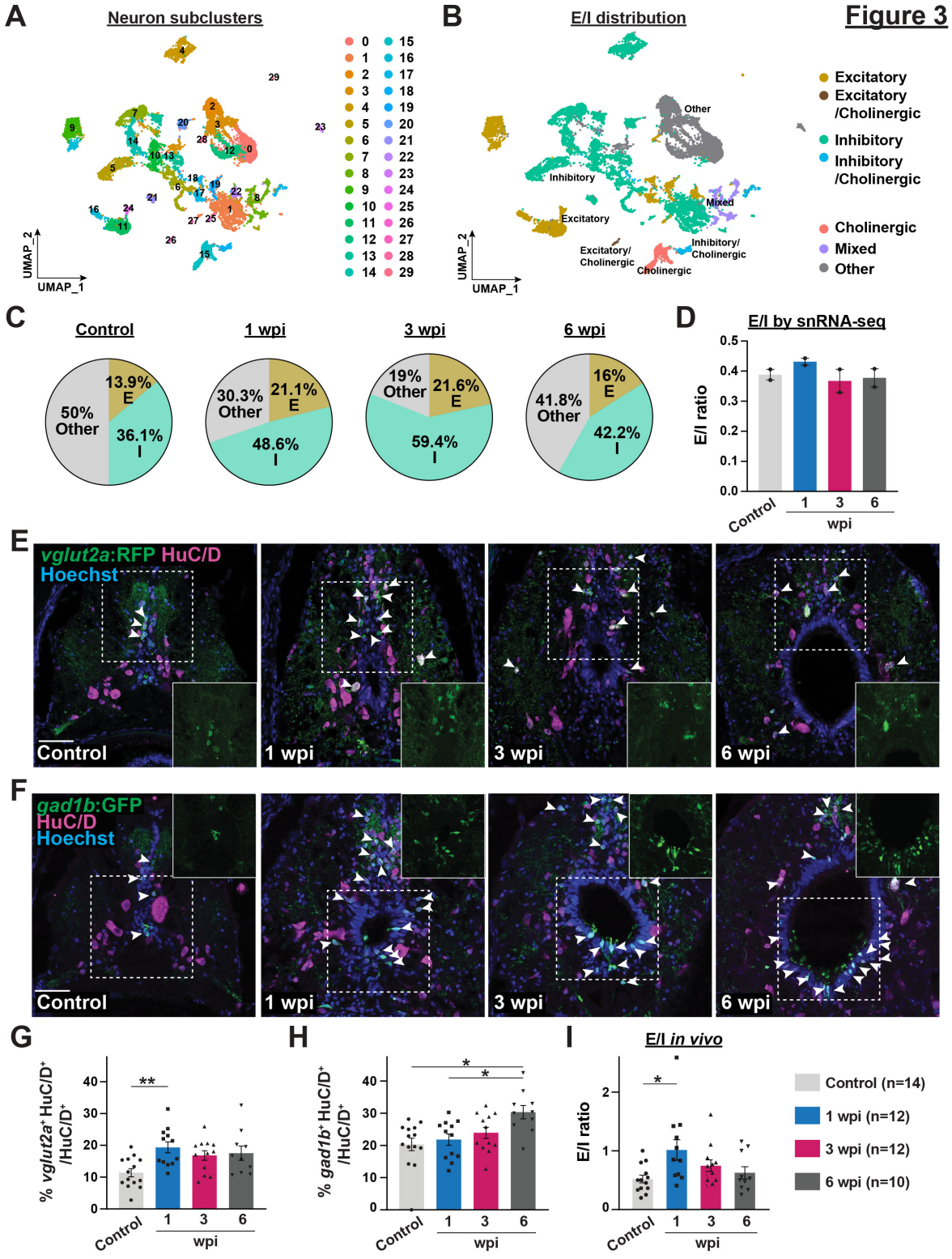
Figure 3
A
Neuron subclusters
UMAP_2
UMAP_1
B
E/I distribution
Excitatory
Excitatory /Cholinergic
Inhibitory
Inhibitory /Cholinergic
Cholinergic
Mixed
Other
Inhibitory
Excitatory
Excitatory/ Cholinergic
Cholinergic
Inhibitory/ Cholinergic
C
Control
1 wpi
3 wpi
6 wpi
50% Other
13.9% E
36.1% I
30.3% Other
21.1% E
48.6% I
19% Other
21.6% E
59.4% I
41.8% Other
16% E
42.2% I
D
E/I by snRNA-seq
E/I ratio
wpi
E
vglut2a:RFP HuC/D
Hoechst
Control
1 wpi
3 wpi
6 wpi
F
gad1b:GFP
HuC/D
Hoechst
Control
1 wpi
3 wpi
6 wpi
G
% vglut2a+ HuC/D+ /HuC/D+
H
% gad1b+ HuC/D+ /HuC/D+
I
E/I in vivo
E/I ratio
Control (n=14)
1 wpi (n=12)
3 wpi (n=12)
6 wpi (n=10)

888 **Figure 3. Recovery of excitatory/inhibitory balance during SC regeneration. (A)** UMAP plot
889 showing 30 different neuron subclusters identified with 0.5 resolution parameter. **(B)** Classification
890 of neuron clusters based on neurotransmitter properties. Canonical neurotransmitter marker
891 genes are used: *slc17a6a* and *slc17a6b* for excitatory neurons; *slc6a5, gad1a, gad1b* and *gad2*
892 for inhibitory neurons, *chata* and *slc5a7a* for cholinergic neurons. Excitatory/cholinergic and
893 inhibitory/cholinergic neurons express cholinergic marker genes along with either excitatory or
894 inhibitory markers, respectively. An ambiguous "Mixed" neuron cluster that expresses excitatory
895 and inhibitory neurotransmitter genes. Neuron subclusters that do not express any of the
896 previously mentioned marker genes are labelled "Other". **(C)** Pie charts show the proportions of
897 excitatory, inhibitory, and "other" neuron populations at 0, 1, 3 and 6 wpi. In this analysis,
898 excitatory neurons comprise excitatory and excitatory/cholinergic neurons. Inhibitory neurons
899 comprise inhibitory and inhibitory/cholinergic neurons. The "Mixed" neuron population was not
900 included in the quantification. **(D)** *in silico* calculation of E/I ratios during SC regeneration. Bar
901 charts depict the ratio between excitatory and inhibitory neurons at 0, 1, 3 and 6 wpi. Dots indicate
902 single biological replicates. Two biological replicates are shown per time point. Error bars
903 represent SEM. **(E,F)** Immunostaining for RFP, GFP, HuC/D and Hoechst in SC cross sections
904 from Tg(*vglut2a*:RFP) and Tg(*gad1b*:GFP) zebrafish at 0, 1, 3 and 6 wpi. White arrows point to
905 RFP^+ HuC/D^+ neurons in E and GFP^+ HuC/D^+ neurons in F. Insets depict single channel views of
906 *vglut2a*:RFP or *gad1b*:GFP in dorsal and ventral SC domains, respectively. **(G,H)** Quantification
907 of glutamatergic and GABAergic neurons after SCI. Percent *vglut2a*$^+$ HuC/D^+ neurons (ANOVA
908 p-value: 0.0086) and *gad1b*$^+$ HuC/D^+ neurons (ANOVA p-value: 0.0043) were normalized to the
909 total number of HuC/D^+ neurons. **(K)** *in vivo* quantification of E/I ratios during SC regeneration.
910 Ratios of glutamatergic to GABAergic neurons were calculated at 0, 1, 3 and 6 wpi (ANOVA p-
911 value: 0.03421). Solid circles and polygons in bar charts indicate individual animals and sample
912 sizes are indicated in parentheses. SC cross sections 450 μm rostral to the lesion were analyzed.
913 Brown-Forsythe and Welch ANOVA test was performed in G, H and I with Dunnett's T3 multiple
914 comparisons test performed across different timepoints having 95% CI. * $p \leq 0.05$, ** $p \leq 0.01$;
915 Scale bars, 50 μm.

Figure 4

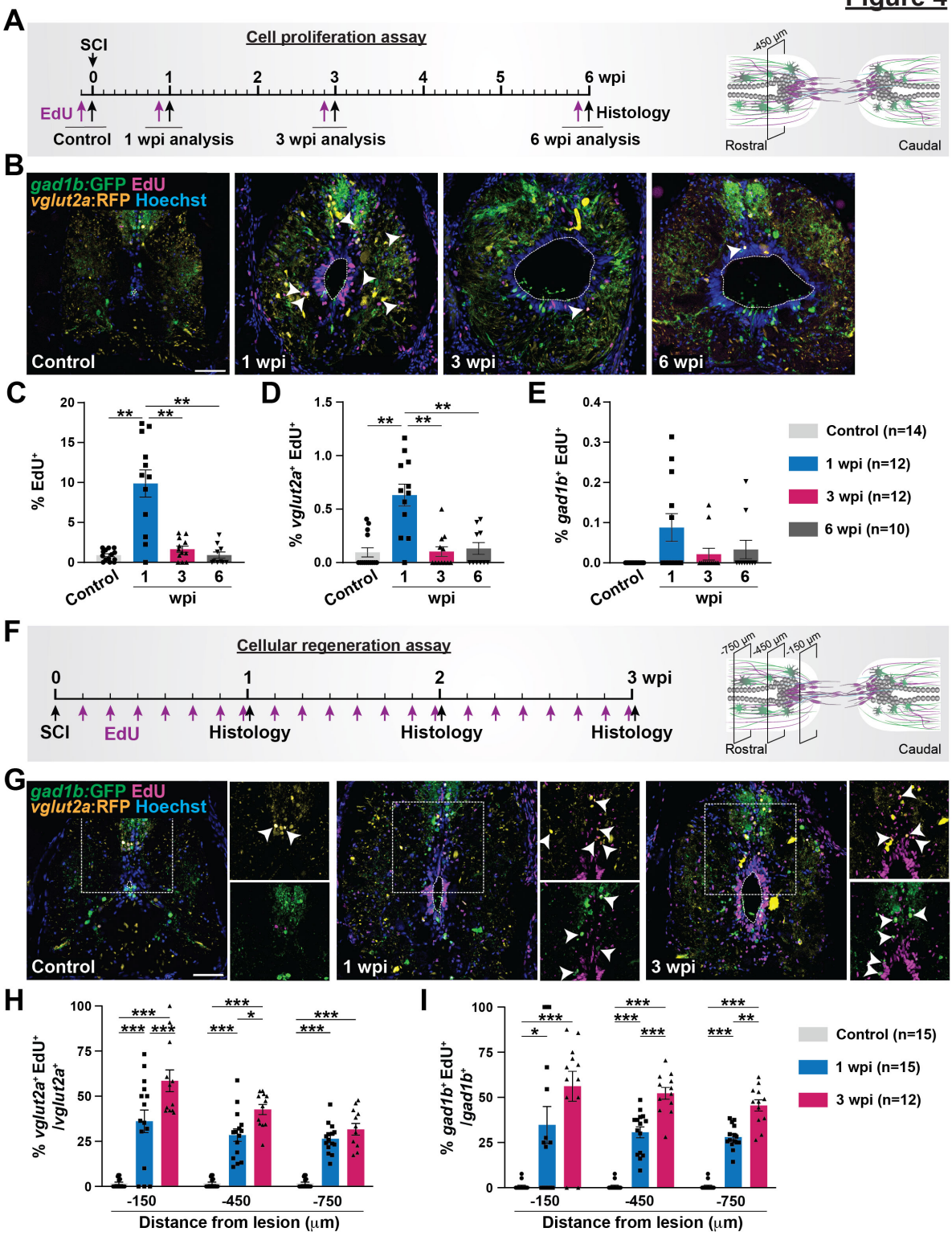
A
Cell proliferation assay
SCI
0
1
2
3
4
5
6 wpi
EdU
Histology
Control
1 wpi analysis
3 wpi analysis
6 wpi analysis
-450 µm
Rostral
Caudal
B
gad1b:GFP EdU
vglut2a:RFP Hoechst
Control
1 wpi
3 wpi
6 wpi
C
% EdU+
Control
1
3
6
wpi
D
% vglut2a+ EdU+
E
% gad1b+ EdU+
Control (n=14)
1 wpi (n=12)
3 wpi (n=12)
6 wpi (n=10)
F
Cellular regeneration assay
0
1
2
3 wpi
SCI
EdU
Histology
-750 µm
-450 µm
-150 µm
G
H
% vglut2a+ EdU+ /vglut2a+
-150
-450
-750
Distance from lesion (µm)
I
% gad1b+ EdU+ /gad1b+
Control (n=15)
1 wpi (n=15)
3 wpi (n=12)

Figure 4. Regeneration of excitatory and inhibitory neurons after SCI. (A) Experimental timeline to assess cell proliferation at 1, 3 and 6 wpi. Tg(*vglut2a*:RFP; *gad1b*:GFP) zebrafish were subjected to SC transections. Single intraperitoneal EdU injections were performed at either 6, 20, or 41 days post-injury. SC tissues were harvested for analysis at 1, 3, or 6 wpi and at 24 hours after EdU injection. Uninjured animals were injected with EdU and collected 24 hours after EdU injection as controls. SC cross-section 450 µm rostral to the lesion was used for quantifications. **(B)** Staining for RFP, GFP, EdU and Hoechst in SC cross sections of Tg(*vglut2a*:RFP; *gad1b*:GFP) zebrafish at 0, 1, 3 and 6 wpi. White arrows indicate *vglut2a*$^+$ EdU$^+$ neurons. Dotted lines delineate central canal edges. **(C-E)** Quantification of EdU$^+$ cells (ANOVA p-value <0.0001), *vglut2a*$^+$ EdU$^+$ neurons (ANOVA p-value <0.0001) and *gad1b*$^+$ EdU$^+$ neurons (ANOVA p-value: 0.0449) at 0, 1, 3 and 6 wpi. Percent cells were normalized to the total number of nuclei in SC sections. **(F)** Experimental timeline to assess the cumulative profiles of regenerating neurons at 1 and 3 wpi. Tg(*vglut2a*:RFP; *gad1b*:GFP) zebrafish were subjected to SC transections and daily intraperitoneal EdU injections. SC tissues were harvested for analysis at 1, 2 or 3 wpi. Control SCs received daily EdU injection for 7 days before collection. Tissue sections 150, 450 and 750 µm rostral to the lesion were analyzed. **(G)** Staining for RFP, GFP, EdU and Hoechst in SC cross sections of Tg(*vglut2a*:RFP; *gad1b*:GFP) zebrafish at 0, 1 and 3 wpi. White arrows indicate *vglut2a*$^+$ EdU$^+$ neurons. Insets show single channel views of *vglut2a*:RFP and *gad1b*:GFP expression. Dotted lines delineate central canal edges. **(H,I)** Quantification of regenerating glutamatergic neurons (*vglut2a*$^+$ EdU$^+$) (ANOVA p-value <0.0001) and regenerating GABAergic neurons (*gad1b*$^+$ EdU$^+$) (ANOVA p-value <0.0001). For each section, percent cells were normalized to the number of *vglut2a*$^+$ EdU$^+$ neurons in H and *vglut2a*$^+$ EdU$^+$ neurons in I. Brown-Forsythe and Welch ANOVA test was performed in C, D and E with Dunnett's T3 multiple comparisons test performed across different time points with 95% CI. Two-way ANOVA was performed in H and I with Tukey's multiple comparison test having 95% CI. * $p \leq 0.05$, ** $p \leq 0.01$, *** $p \leq 0.001$. Solid circles and polygons in the bar charts indicate individual animals and sample sizes are indicated in parentheses. Scale bars, 50 µm.

Figure 5

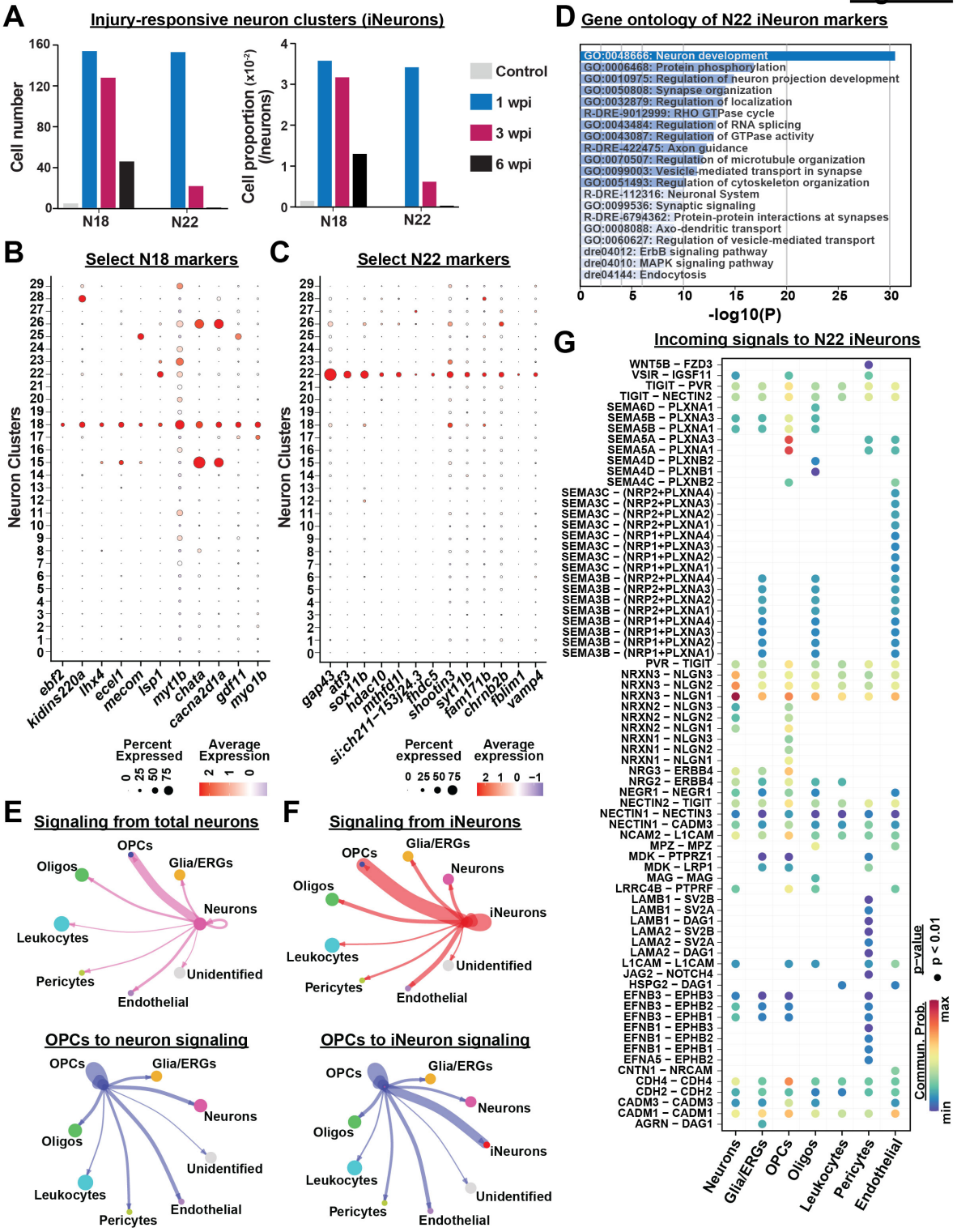
A
Injury-responsive neuron clusters (iNeurons)
Cell number
Cell proportion (x10⁻²) (/neurons)
N18
N22
Control
1 wpi
3 wpi
6 wpi
B
Select N18 markers
C
Select N22 markers
Neuron Clusters
ebf2
kidins220a
lhx4
ecel1
mecom
lsp1
myt1b
chata
cacna2d1a
gdf11
myo1b
gap43
atf3
sox11b
hdac10
mthfd1l
si:ch211-153j24.3
fhdc5
shootin3
syt11b
fam171b
chrnb2b
fblim1
vamp4
Percent Expressed
Average Expression
Percent expressed
Average expression
D
Gene ontology of N22 iNeuron markers
GO:0048666: Neuron development
GO:0006468: Protein phosphorylation
GO:0010975: Regulation of neuron projection development
GO:0050808: Synapse organization
GO:0032879: Regulation of localization
R-DRE-9012999: RHO GTPase cycle
GO:0043484: Regulation of RNA splicing
GO:0043087: Regulation of GTPase activity
R-DRE-422475: Axon guidance
GO:0070507: Regulation of microtubule organization
GO:0099003: Vesicle-mediated transport in synapse
GO:0051493: Regulation of cytoskeleton organization
R-DRE-112316: Neuronal System
GO:0099536: Synaptic signaling
R-DRE-6794362: Protein-protein interactions at synapses
GO:0008088: Axo-dendritic transport
GO:0060627: Regulation of vesicle-mediated transport
dre04012: ErbB signaling pathway
dre04010: MAPK signaling pathway
dre04144: Endocytosis
-log10(P)
E
Signaling from total neurons
OPCs
Glia/ERGs
Oligos
Neurons
Leukocytes
Pericytes
Unidentified
Endothelial
OPCs to neuron signaling
F
Signaling from iNeurons
iNeurons
OPCs to iNeuron signaling
G
Incoming signals to N22 iNeurons
WNT5B – FZD3
VSIR – IGSF11
TIGIT – PVR
TIGIT – NECTIN2
SEMA6D – PLXNA1
SEMA5B – PLXNA3
SEMA5B – PLXNA1
SEMA5A – PLXNA3
SEMA5A – PLXNA1
SEMA4D – PLXNB2
SEMA4D – PLXNB1
SEMA4C – PLXNB2
SEMA3C – (NRP2+PLXNA4)
SEMA3C – (NRP2+PLXNA3)
SEMA3C – (NRP2+PLXNA2)
SEMA3C – (NRP2+PLXNA1)
SEMA3C – (NRP1+PLXNA4)
SEMA3C – (NRP1+PLXNA3)
SEMA3C – (NRP1+PLXNA2)
SEMA3C – (NRP1+PLXNA1)
SEMA3B – (NRP2+PLXNA4)
SEMA3B – (NRP2+PLXNA3)
SEMA3B – (NRP2+PLXNA2)
SEMA3B – (NRP2+PLXNA1)
SEMA3B – (NRP1+PLXNA4)
SEMA3B – (NRP1+PLXNA3)
SEMA3B – (NRP1+PLXNA2)
SEMA3B – (NRP1+PLXNA1)
PVR – TIGIT
NRXN3 – NLGN3
NRXN3 – NLGN2
NRXN3 – NLGN1
NRXN2 – NLGN3
NRXN2 – NLGN2
NRXN2 – NLGN1
NRXN1 – NLGN3
NRXN1 – NLGN2
NRXN1 – NLGN1
NRG3 – ERBB4
NRG2 – ERBB4
NEGR1 – NEGR1
NECTIN2 – TIGIT
NECTIN1 – NECTIN3
NECTIN1 – CADM3
NCAM2 – L1CAM
MPZ – MPZ
MDK – PTPRZ1
MDK – LRP1
MAG – MAG
LRRC4B – PTPRF
LAMB1 – SV2B
LAMB1 – SV2A
LAMB1 – DAG1
LAMA2 – SV2B
LAMA2 – SV2A
LAMA2 – DAG1
L1CAM – L1CAM
JAG2 – NOTCH4
HSPG2 – DAG1
EFNB3 – EPHB3
EFNB3 – EPHB2
EFNB3 – EPHB1
EFNB1 – EPHB3
EFNB1 – EPHB2
EFNB1 – EPHB1
EFNA5 – EPHB2
CNTN1 – NRCAM
CDH4 – CDH4
CDH2 – CDH2
CADM3 – CADM3
CADM1 – CADM1
AGRN – DAG1
p-value
p < 0.01
Commun. Prob.
max
min

943 **Figure 5. Emergence of an injury-responsive iNeuron signature during SC regeneration.**
944 **(A)** Numbers and proportions of N18 and N22 iNeurons at 0, 1, 3 and 6 wpi. **(B,C)** Marker gene
945 expression for N18 (B) and N22 iNeurons (C). Dot plot shows select DE marker genes. Dot colors
946 and diameters represent average gene expression and percent cells with at least one UMI
947 detected per gene, respectively. **(D)** Gene ontology of N22 iNeuron DE markers. Twenty of the
948 most enriched terms are shown. X-axis represents -log10(p-value) for each term. **(E,F)** Circle
949 plots represent cell-cell interaction strengths at 6 wpi. Signaling pathways outgoing from total
950 neurons and from OPCs to total neurons are shown in E. Signaling pathways outgoing from
951 iNeurons and from OPCs to iNeurons are shown in F. Arrow thickness is directly proportional to
952 the cumulative strengths of all predicted interactions between clusters. **(G)** Bubble plot shows
953 significant ligand-receptor interaction pair of signaling pathways incoming to iNeurons at 1 wpi.
954 Dot colors and diameters represent interaction probabilities and p-values, respectively.

Figure 6

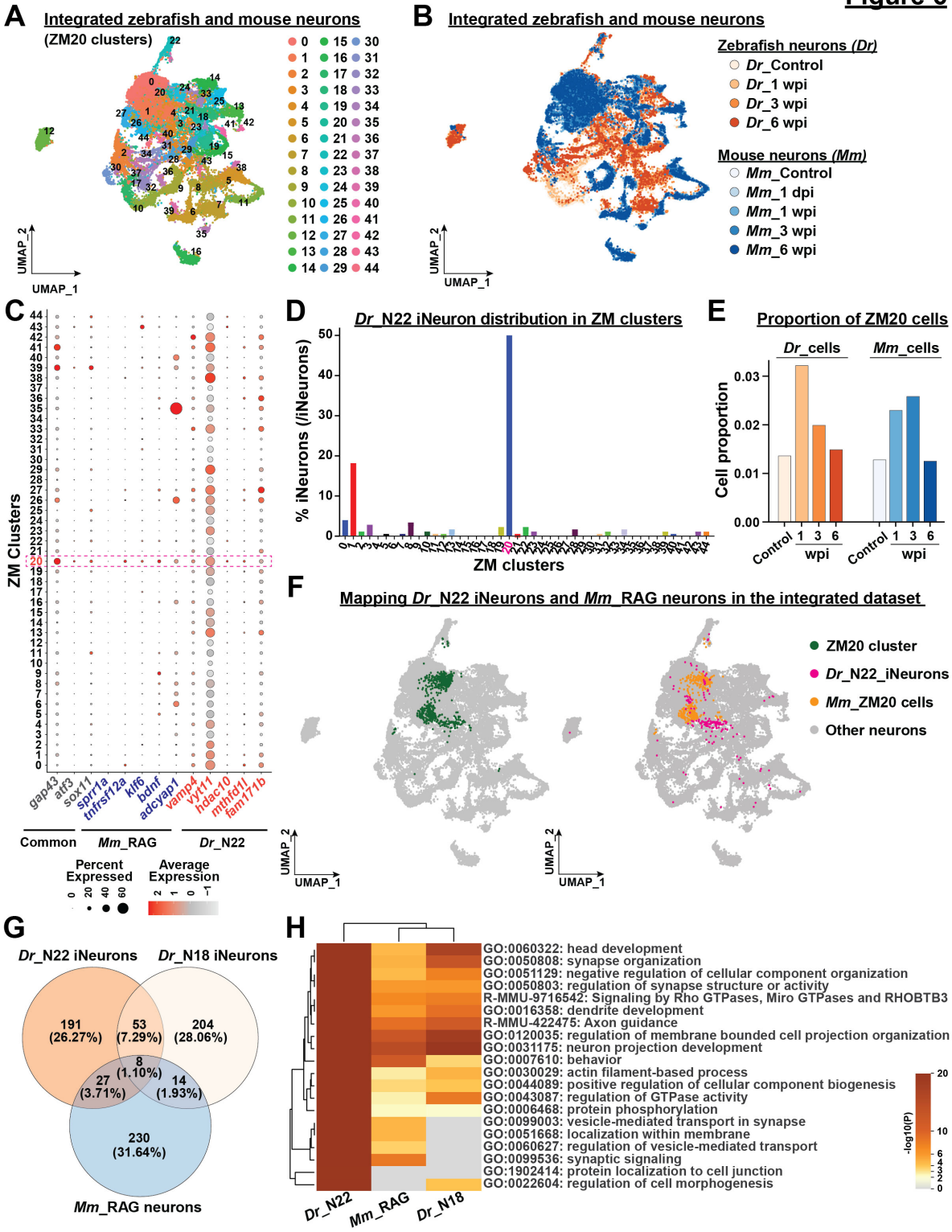
A
Integrated zebrafish and mouse neurons
(ZM20 clusters)
UMAP_1
UMAP_2
B
Integrated zebrafish and mouse neurons
Zebrafish neurons (Dr)
Dr_Control
Dr_1 wpi
Dr_3 wpi
Dr_6 wpi
Mouse neurons (Mm)
Mm_Control
Mm_1 dpi
Mm_1 wpi
Mm_3 wpi
Mm_6 wpi
C
ZM Clusters
gap43
atf3
sox11
sprr1a
tnfrsf12a
klf6
bdnf
adcyap1
vamp4
vyt11
hdac10
mthfd1l
fam171b
Common
Mm_RAG
Dr_N22
Percent Expressed
Average Expression
D
Dr_N22 iNeuron distribution in ZM clusters
% iNeurons (/iNeurons)
ZM clusters
E
Proportion of ZM20 cells
Dr_cells
Mm_cells
Cell proportion
Control
wpi
F
Mapping Dr_N22 iNeurons and Mm_RAG neurons in the integrated dataset
ZM20 cluster
Dr_N22_iNeurons
Mm_ZM20 cells
Other neurons
G
Dr_N22 iNeurons
Dr_N18 iNeurons
191 (26.27%)
53 (7.29%)
204 (28.06%)
8 (1.10%)
27 (3.71%)
14 (1.93%)
230 (31.64%)
Mm_RAG neurons
H
GO:0060322: head development
GO:0050808: synapse organization
GO:0051129: negative regulation of cellular component organization
GO:0050803: regulation of synapse structure or activity
R-MMU-9716542: Signaling by Rho GTPases, Miro GTPases and RHOBTB3
GO:0016358: dendrite development
R-MMU-422475: Axon guidance
GO:0120035: regulation of membrane bounded cell projection organization
GO:0031175: neuron projection development
GO:0007610: behavior
GO:0030029: actin filament-based process
GO:0044089: positive regulation of cellular component biogenesis
GO:0043087: regulation of GTPase activity
GO:0006468: protein phosphorylation
GO:0099003: vesicle-mediated transport in synapse
GO:0051668: localization within membrane
GO:0060627: regulation of vesicle-mediated transport
GO:0099536: synaptic signaling
GO:1902414: protein localization to cell junction
GO:0022604: regulation of cell morphogenesis
-log10(P)
Dr_N22
Mm_RAG
Dr_N18

955 **Figure 6. Cross-species transcriptional comparisons between zebrafish and mouse**
956 **neurons. (A,B)** UMAP plot showing 45 distinct clusters in the integrated ZM dataset of mouse
957 (*Mm*) and zebrafish (*Dr*) neurons at 1.1 resolution parameter. Dot colors represent cluster identity
958 in A and the species of origin of each cell in B. **(C)** Dot plot represent the expression of N22
959 iNeuron and mouse RAG marker genes in the integrated ZM datset. Dot colors and diameters
960 represent average gene expression and percent cells with at least one UMI detected per gene,
961 respectively. Cluster ZM20 of the integrated ZM dataset shows enriched expression of 12/13
962 genes, and is highlighted in the dotted rectangular box. **(D)** Distribution of N22 iNeurons in the
963 integrated ZM dataset. Cluster ZM 20 shows the highest proportion of N22 iNeurons and is
964 highlighted in magenta. **(E)** Proportion of cluster ZM20 cells in the zebrafish and mouse datasets
965 at different time points after SCI. **(F)** UMAP plots highlight zebrafish N22 iNeurons and mouse
966 RAG neurons in the integrated ZM dataset. **(G)** Venn diagram ccomparing the top DE markers of
967 zebrafish N22 iNeurons, zebrafish N18 iNeurons and mouse RAG neurons. The numbers and
968 proportions of genes are shown for each section. **(H)** Gene ontology for the top DE markers of
969 zebrafish N22 iNeurons, and zebrafish N18 iNeurons and mouse RAG neurons. Color gradients
970 indicate -log10(p-value). Dendrograms on the left and top of the heatmap represent hierarchical
971 clustering of GO terms.

Figure 7

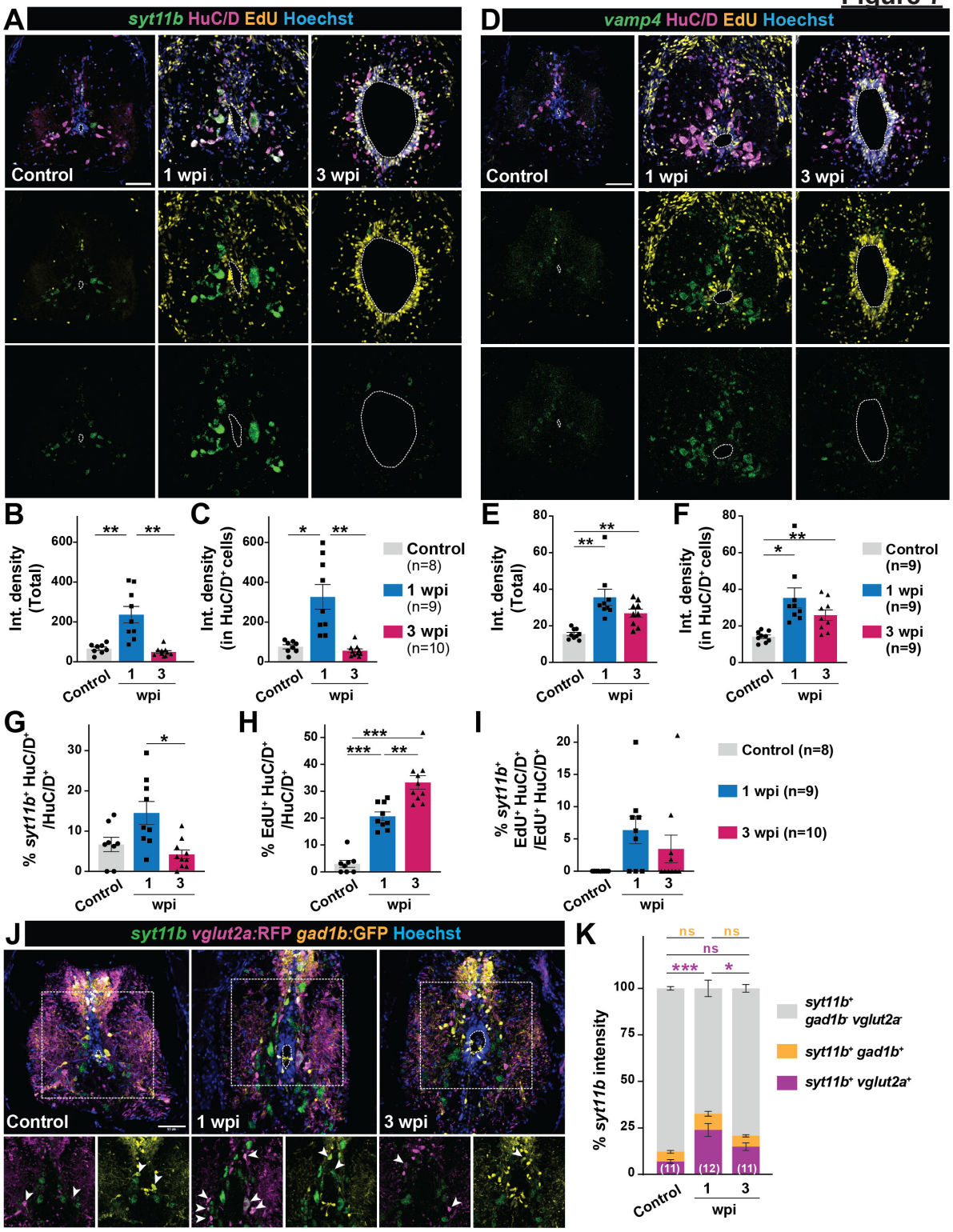
A
syt11b HuC/D EdU Hoechst
Control
1 wpi
3 wpi
D
vamp4 HuC/D EdU Hoechst
Control
1 wpi
3 wpi
B
Int. density (Total)
Control
1
3
wpi
C
Int. density (in HuC/D+ cells)
Control (n=8)
1 wpi (n=9)
3 wpi (n=10)
E
Int. density (Total)
F
Int. density (in HuC/D+ cells)
Control (n=9)
1 wpi (n=9)
3 wpi (n=9)
G
% syt11b+ HuC/D+ /HuC/D+
H
% EdU+ HuC/D+ /HuC/D+
I
% syt11b+ EdU+ HuC/D+ /EdU+ HuC/D+
Control (n=8)
1 wpi (n=9)
3 wpi (n=10)
J
syt11b vglut2a:RFP gad1b:GFP Hoechst
Control
1 wpi
3 wpi
K
% syt11b intensity
ns
***
*
(11)
(12)
(11)
syt11b+ gad1b- vglut2a-
syt11b+ gad1b+
syt11b+ vglut2a+

Figure 7. *in vivo* mapping of N22 iNeurons in zebrafish spinal tissues. (A) HCR *in situ* hybridization for *syt11b* and staining for HuC/D, Hoechst and EdU were performed on wild-type SC cross sections at 0, 1 and 3 wpi. Dotted lines delineate central canal edges. **(B,C)** Quantification of *syt11b* HCR *in situ* hybridization. Integrated density was calculated in the whole SC cross sections (ANOVA p-value: 0.0007) and inside HuC/D$^+$ neurons (ANOVA p-value: 0.0009) at 0, 1 and 3 wpi. **(D)** HCR *in situ* hybridization for *vamp4* and staining for HuC/D, Hoechst and EdU were performed on wild-type SC cross sections at 0, 1 and 3 wpi. Dotted lines delineate central canal edges. **(E,F)** Quantification of *vamp4* HCR *in situ* hybridization. Integrated density was calculated in the whole SC cross sections (ANOVA p-value: 0.0012) and inside HuC/D$^+$ neurons (ANOVA p-value: 0.0043) at 0, 1 and 3 wpi. **(G-I)** Quantification of *syt11b* expressing cells after SCI. Percent *syt11b*$^+$ HuC/D$^+$ neurons (normalized to HuC/D$^+$ neurons in G) (ANOVA p-value: 0.0062), percent EdU$^+$ HuC/D$^+$ neurons (normalized to HuC/D$^+$ neurons in H) (ANOVA p-value <0.0001), and percent *syt11b*$^+$ EdU$^+$ HuC/D$^+$ neurons (normalized to EdU$^+$ HuC/D$^+$ neurons in I) (ANOVA p-value: 0.0813). Analysis was performed on whole SC cross sections at 0, 1 and 3 wpi. **(J)** HCR *in situ* hybridization for *syt11b* in SC cross-sections of Tg(*vglut2a*:RFP; *gad1b*:GFP) zebrafish at 0, 1 and 3 wpi. Dotted lines delineate central canal edges. White arrowheads point to overlapping of *syt11b* transcripts with either *vglut2a* or *gad1b*. **(K)** Quantification of *syt11b* transcripts within *vglut2a*$^+$ and *gad1b*$^+$ neurons at 0, 1 and 3 wpi (ANOVA p-value <0.0001). *syt11b* signal outside either of these neurotransmitter populations was also quantified. SC cross sections at 450 µm rostral to the lesion were analyzed. Solid circles and polygons in the bar charts indicate individual animals and sample sizes are indicated in parentheses. Brown-Forsythe and Welch ANOVA test was performed in B, C, E, F, G, H, and I with Dunnett's T3 multiple comparisons test performed across different timepoints with 95% CI. Two-way ANOVA was performed in K with Tukey's multiple comparisons test with 95 % CI. * p≤0.05, ** p ≤0.01, *** p≤0.001. Scale bars, 50 µm**.**

Figure 8

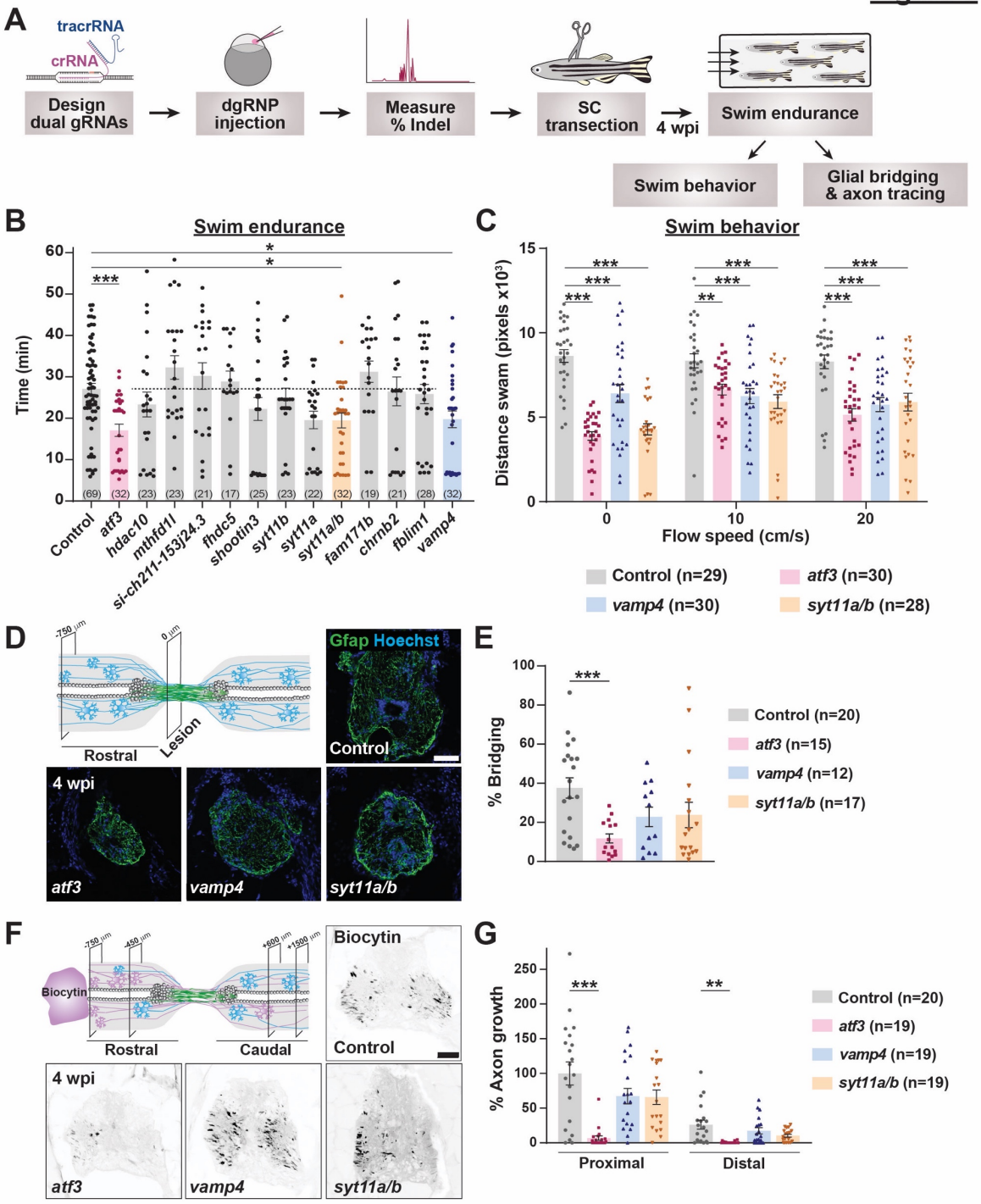
A
tracrRNA
crRNA
Design dual gRNAs
dgRNP injection
Measure % Indel
SC transection
4 wpi
Swim endurance
Swim behavior
Glial bridging & axon tracing
B
Swim endurance
Time (min)
Control
atf3
hdac10
mthfd1l
si-ch211-153j24.3
fhdc5
shootin3
syt11b
syt11a
syt11a/b
fam171b
chrnb2
fblim1
vamp4
C
Swim behavior
Distance swam (pixels x10³)
Flow speed (cm/s)
Control (n=29)
atf3 (n=30)
vamp4 (n=30)
syt11a/b (n=28)
D
Rostral
Lesion
Gfap Hoechst
Control
4 wpi
atf3
vamp4
syt11a/b
E
% Bridging
Control (n=20)
atf3 (n=15)
vamp4 (n=12)
syt11a/b (n=17)
F
Biocytin
Rostral
Caudal
Control
4 wpi
atf3
vamp4
syt11a/b
G
% Axon growth
Proximal
Distal
Control (n=20)
atf3 (n=19)
vamp4 (n=19)
syt11a/b (n=19)

Figure 8. CRISPR/Cas9 mutagenesis of N22 iNeuron marker genes in zebrafish. (A) Pipeline for CRISPR/Cas9 mutagenesis of N22 iNeuron marker genes for regeneration assessment. CRISPR/Cas9 dual-guide ribonucleic protein duplexes targeting iNeuron genes injected into one-cell zebrafish embryos. Mutagenesis efficiency was confirmed by capillary electrophoresis and animals with >90% mutagenesis were used for SCI. Swim endurance, swim behavior and histological regeneration assays were performed at 4 wpi. **(B)** Functional recovery in CRISPR/Cas9 targeted animals 4 wpi. For each group of targeted animals, uninjected siblings were subjected to SCI and swim endurance assays (ANOVA p-value <0.0001). Dots represent individual animals. The black dotted line marks average swim time in control animals. **(C)** Swim behavior assays in CRISPR/Cas9 targeted animals 4 wpi (ANOVA p-value <0.0001). Swim distance was tracked under water current velocities of 0, 10 and 20 cm/s. **(D,E)** Glial bridging in CRISPR/Cas9 targeted animals at 4 wpi. Representative immunohistochemistry shows the $Gfap^+$ bridge at the lesion site in *atf3, vamp4* and *syt11a/b* crispants relative to controls. Percent bridging represents the cross-sectional area of the glial bridge at the lesion site relative to the intact SC (ANOVA p-value: 0.0049). **(F,G)** Anterograde axon tracing in CRISPR/Cas9 targeted animals at 4 wpi. Biocytin axon tracer was applied rostrally and analyzed at 600 μm (proximal) (ANOVA p-value <0.0001) and 1500 μm (distal) (ANOVA p-value: 0.0006) caudal to the lesion. Representative traces of biocytin are shown at the proximal level. Axon regrowth was normalized to biocytin labeling in wild-type controls at the proximal level. Solid circles and polygons in the bar charts indicate individual animal and sample sizes are indicated in parentheses. Brown-Forsythe and Welch ANOVA test was performed in B, E and G with Dunnett's T3 multiple comparisons test performed across different time points with 95% CI. Two-way ANOVA with Dunnett's multiple comparisons test (95% CI) was performed in C. * $p \leq 0.05$, ** $p \leq 0.01$, *** $p \leq 0.001$. Scale bars, 50 μm.

REFERENCES

Ahlmann-Eltze, C. and Huber, W. (2021) 'glmGamPoi: fitting Gamma-Poisson generalized linear models on single cell count data', *Bioinformatics* 36(24): 5701-5702.

Anderson, M. A., O'Shea, T. M., Burda, J. E., Ao, Y., Barlatey, S. L., Bernstein, A. M., Kim, J. H., James, N. D., Rogers, A., Kato, B. et al. (2018) 'Required growth facilitators propel axon regeneration across complete spinal cord injury', *Nature* 561(7723): 396-400.

Baek, M., Menon, V., Jessell, T. M., Hantman, A. W. and Dasen, J. S. (2019) 'Molecular Logic of Spinocerebellar Tract Neuron Diversity and Connectivity', *Cell Rep* 27(9): 2620-2635 e4.

Bakken, T. E., Hodge, R. D., Miller, J. A., Yao, Z., Nguyen, T. N., Aevermann, B., Barkan, E., Bertagnolli, D., Casper, T., Dee, N. et al. (2018) 'Single-nucleus and single-cell transcriptomes compared in matched cortical cell types', *PLoS One* 13(12): e0209648.

Bakr, M., Jullie, D., Krapivkina, J., Paget-Blanc, V., Bouit, L., Petersen, J. D., Retailleau, N., Breillat, C., Herzog, E., Choquet, D. et al. (2021) 'The vSNAREs VAMP2 and VAMP4 control recycling and intracellular sorting of post-synaptic receptors in neuronal dendrites', *Cell Rep* 36(10): 109678.

Bartus, K., Burnside, E. R., Galino, J., James, N. D., Bennett, D. L. H. and Bradbury, E. J. (2019) 'ErbB receptor signaling directly controls oligodendrocyte progenitor cell transformation and spontaneous remyelination after spinal cord injury', *Glia* 67(6): 1036-1046.

Becht, E., McInnes, L., Healy, J., Dutertre, C. A., Kwok, I. W. H., Ng, L. G., Ginhoux, F. and Newell, E. W. (2018) 'Dimensionality reduction for visualizing single-cell data using UMAP', *Nat Biotechnol*.

Becker, C. G., Schweitzer, J., Feldner, J., Schachner, M. and Becker, T. (2004) 'Tenascin-R as a repellent guidance molecule for newly growing and regenerating optic axons in adult zebrafish', *Mol Cell Neurosci* 26(3): 376-89.

Bernhardt, R. R., Tongiorgi, E., Anzini, P. and Schachner, M. (1996) 'Increased expression of specific recognition molecules by retinal ganglion cells and by optic pathway glia accompanies the successful regeneration of retinal axons in adult zebrafish', *J Comp Neurol* 376(2): 253-64.

Bertels, H., Vicente-Ortiz, G., El Kanbi, K. and Takeoka, A. (2022) 'Neurotransmitter phenotype switching by spinal excitatory interneurons regulates locomotor recovery after spinal cord injury', *Nat Neurosci* 25(5): 617-629.

Bertuzzi, M., Chang, W. and Ampatzis, K. (2018) 'Adult spinal motoneurons change their neurotransmitter phenotype to control locomotion', *Proc Natl Acad Sci U S A* 115(42): E9926-E9933.

Brennan, F. H. and Popovich, P. G. (2018) 'Emerging targets for reprograming the immune response to promote repair and recovery of function after spinal cord injury', *Curr Opin Neurol* 31(3): 334-344.

Briona, L. K., Poulain, F. E., Mosimann, C. and Dorsky, R. I. (2015) 'Wnt/ss-catenin signaling is required for radial glial neurogenesis following spinal cord injury', *Dev Biol* 403(1): 15-21.

1033 Burris, B., Jensen, N. and Mokalled, M. H. (2021) 'Assessment of Swim Endurance and Swim
1034 Behavior in Adult Zebrafish', *Journal of visualized experiments : JoVE*(177).

1035 Busch, S. A. and Silver, J. (2007) 'The role of extracellular matrix in CNS regeneration', *Curr Opin*
1036 *Neurobiol* 17(1): 120-7.

1037 Butler, A., Hoffman, P., Smibert, P., Papalexi, E. and Satija, R. (2018) 'Integrating single-cell
1038 transcriptomic data across different conditions, technologies, and species', *Nat Biotechnol* 36(5):
1039 411-420.

1040 Cavone, L., McCann, T., Drake, L. K., Aguzzi, E. A., Oprisoreanu, A. M., Pedersen, E., Sandi, S.,
1041 Selvarajah, J., Tsarouchas, T. M., Wehner, D. et al. (2021) 'A unique macrophage subpopulation
1042 signals directly to progenitor cells to promote regenerative neurogenesis in the zebrafish spinal
1043 cord', *Developmental cell* 56(11): 1617-1630 e6.

1044 Choi, H. M. T., Schwarzkopf, M., Fornace, M. E., Acharya, A., Artavanis, G., Stegmaier, J., Cunha,
1045 A. and Pierce, N. A. (2018) 'Third-generation in situ hybridization chain reaction: multiplexed,
1046 quantitative, sensitive, versatile, robust', *Development* 145(12).

1047 Cohen, T., Gluzman-Poltorak, Z., Brodzky, A., Meytal, V., Sabo, E., Misselevich, I., Hassoun, M.,
1048 Boss, J. H., Resnick, M., Shneyvas, D. et al. (2001) 'Neuroendocrine cells along the digestive
1049 tract express neuropilin-2', *Biochem Biophys Res Commun* 284(2): 395-403.

1050 DePaul, M. A., Lin, C. Y., Silver, J. and Lee, Y. S. (2017) 'Combinatory repair strategy to promote
1051 axon regeneration and functional recovery after chronic spinal cord injury', *Sci Rep* 7(1): 9018.

1052 Dias, T. B., Yang, Y. J., Ogai, K., Becker, T. and Becker, C. G. (2012) 'Notch signaling controls
1053 generation of motor neurons in the lesioned spinal cord of adult zebrafish', *J Neurosci* 32(9): 3245-
1054 52.

1055 Ding, J., Adiconis, X., Simmons, S. K., Kowalczyk, M. S., Hession, C. C., Marjanovic, N. D.,
1056 Hughes, T. K., Wadsworth, M. H., Burks, T., Nguyen, L. T. et al. (2020) 'Systematic comparison
1057 of single-cell and single-nucleus RNA-sequencing methods', *Nat Biotechnol* 38(6): 737-746.

1058 Dudek, F. E. and Sutula, T. P. (2007) 'Epileptogenesis in the dentate gyrus: a critical perspective',
1059 *Prog Brain Res* 163: 755-73.

1060 Durinck, S., Spellman, P. T., Birney, E. and Huber, W. (2009) 'Mapping identifiers for the
1061 integration of genomic datasets with the R/Bioconductor package biomaRt', *Nat Protoc* 4(8):
1062 1184-91.

1063 Falk, J., Bechara, A., Fiore, R., Nawabi, H., Zhou, H., Hoyo-Becerra, C., Bozon, M., Rougon, G.,
1064 Grumet, M., Puschel, A. W. et al. (2005) 'Dual functional activity of semaphorin 3B is required for
1065 positioning the anterior commissure', *Neuron* 48(1): 63-75.

1066 Ferrario, J. E., Baskaran, P., Clark, C., Hendry, A., Lerner, O., Hintze, M., Allen, J., Chilton, J. K.
1067 and Guthrie, S. (2012) 'Axon guidance in the developing ocular motor system and Duane
1068 retraction syndrome depends on Semaphorin signaling via alpha2-chimaerin', *Proc Natl Acad Sci*
1069 *U S A* 109(36): 14669-74.

1070 Fouad, K., Popovich, P. G., Kopp, M. A. and Schwab, J. M. (2021) 'The neuroanatomical-
1071 functional paradox in spinal cord injury', *Nat Rev Neurol* 17(1): 53-62.

1072 Gao, R. and Penzes, P. (2015) 'Common mechanisms of excitatory and inhibitory imbalance in
1073 schizophrenia and autism spectrum disorders', *Curr Mol Med* 15(2): 146-67.

1074 Gey, M., Wanner, R., Schilling, C., Pedro, M. T., Sinske, D. and Knoll, B. (2016) 'Atf3 mutant mice
1075 show reduced axon regeneration and impaired regeneration-associated gene induction after
1076 peripheral nerve injury', *Open Biol* 6(8).

1077 Goldshmit, Y., Sztal, T. E., Jusuf, P. R., Hall, T. E., Nguyen-Chi, M. and Currie, P. D. (2012) 'Fgf-
1078 dependent glial cell bridges facilitate spinal cord regeneration in zebrafish', *J Neurosci* 32(22):
1079 7477-92.

1080 Guillemot, F. (2007) 'Spatial and temporal specification of neural fates by transcription factor
1081 codes', *Development* 134(21): 3771-80.

1082 Gulati, G. S., Sikandar, S. S., Wesche, D. J., Manjunath, A., Bharadwaj, A., Berger, M. J., Ilagan,
1083 F., Kuo, A. H., Hsieh, R. W., Cai, S. et al. (2020) 'Single-cell transcriptional diversity is a hallmark
1084 of developmental potential', *Science* 367(6476): 405-411.

1085 Haenisch, C., Diekmann, H., Klinger, M., Gennarini, G., Kuwada, J. Y. and Stuermer, C. A. (2005)
1086 'The neuronal growth and regeneration associated Cntn1 (F3/F11/Contactin) gene is duplicated
1087 in fish: expression during development and retinal axon regeneration', *Mol Cell Neurosci* 28(2):
1088 361-74.

1089 Hafemeister, C. and Satija, R. (2019) 'Normalization and variance stabilization of single-cell RNA-
1090 seq data using regularized negative binomial regression', *Genome Biol* 20(1): 296.

1091 Haghverdi, L., Lun, A. T. L., Morgan, M. D. and Marioni, J. C. (2018) 'Batch effects in single-cell
1092 RNA-sequencing data are corrected by matching mutual nearest neighbors', *Nat Biotechnol*
1093 36(5): 421-427.

1094 Haring, M., Zeisel, A., Hochgerner, H., Rinwa, P., Jakobsson, J. E. T., Lonnerberg, P., La Manno,
1095 G., Sharma, N., Borgius, L., Kiehn, O. et al. (2018) 'Neuronal atlas of the dorsal horn defines its
1096 architecture and links sensory input to transcriptional cell types', *Nat Neurosci* 21(6): 869-880.

1097 Hayashi, M., Hinckley, C. A., Driscoll, S. P., Moore, N. J., Levine, A. J., Hilde, K. L., Sharma, K.
1098 and Pfaff, S. L. (2018) 'Graded Arrays of Spinal and Supraspinal V2a Interneuron Subtypes
1099 Underlie Forelimb and Hindlimb Motor Control', *Neuron* 97(4): 869-884 e5.

1100 He, Z. and Jin, Y. (2016) 'Intrinsic Control of Axon Regeneration', *Neuron* 90(3): 437-51.

1101 Hernandez-Miranda, L. R., Muller, T. and Birchmeier, C. (2017) 'The dorsal spinal cord and
1102 hindbrain: From developmental mechanisms to functional circuits', *Dev Biol* 432(1): 34-42.

1103 Hilton, B. J., Husch, A., Schaffran, B., Lin, T. C., Burnside, E. R., Dupraz, S., Schelski, M., Kim,
1104 J., Muller, J. A., Schoch, S. et al. (2022) 'An active vesicle priming machinery suppresses axon
1105 regeneration upon adult CNS injury', *Neuron* 110(1): 51-69 e7.

1106 Hou, J., Bi, H., Ge, Q., Teng, H., Wan, G., Yu, B., Jiang, Q. and Gu, X. (2022) 'Heterogeneity
1107 analysis of astrocytes following spinal cord injury at single-cell resolution', *FASEB J* 36(8):
1108 e22442.

1109 Huang, C. X., Zhao, Y., Mao, J., Wang, Z., Xu, L., Cheng, J., Guan, N. N. and Song, J. (2021) 'An
1110 injury-induced serotonergic neuron subpopulation contributes to axon regrowth and function
1111 restoration after spinal cord injury in zebrafish', *Nat Commun* 12(1): 7093.

1112 Ilicic, T., Kim, J. K., Kolodziejczyk, A. A., Bagger, F. O., McCarthy, D. J., Marioni, J. C. and
1113 Teichmann, S. A. (2016) 'Classification of low quality cells from single-cell RNA-seq data',
1114 *Genome Biol* 17: 29.

1115 Isaacson, J. S. and Scanziani, M. (2011) 'How inhibition shapes cortical activity', *Neuron* 72(2):
1116 231-43.

1117 Jankowski, M. P., McIlwrath, S. L., Jing, X., Cornuet, P. K., Salerno, K. M., Koerber, H. R. and
1118 Albers, K. M. (2009) 'Sox11 transcription factor modulates peripheral nerve regeneration in adult
1119 mice', *Brain Res* 1256: 43-54.

1120 Jin, S., Guerrero-Juarez, C. F., Zhang, L., Chang, I., Ramos, R., Kuan, C. H., Myung, P., Plikus,
1121 M. V. and Nie, Q. (2021) 'Inference and analysis of cell-cell communication using CellChat', *Nat*
1122 *Commun* 12(1): 1088.

1123 Jing, X., Wang, T., Huang, S., Glorioso, J. C. and Albers, K. M. (2012) 'The transcription factor
1124 Sox11 promotes nerve regeneration through activation of the regeneration-associated gene
1125 Sprr1a', *Exp Neurol* 233(1): 221-32.

1126 Jung, M., Petrausch, B. and Stuermer, C. A. (1997) 'Axon-regenerating retinal ganglion cells in
1127 adult rats synthesize the cell adhesion molecule L1 but not TAG-1 or SC-1', *Mol Cell Neurosci*
1128 9(2): 116-31.

1129 Klatt Shaw, D. and Mokalled, M. H. (2021) 'Efficient CRISPR/Cas9 mutagenesis for
1130 neurobehavioral screening in adult zebrafish', *G3 (Bethesda)* 11(8).

1131 Klatt Shaw, D., Saraswathy, V. M., Zhou, L., McAdow, A. R., Burris, B., Butka, E., Morris, S. A.,
1132 Dietmann, S. and Mokalled, M. H. (2021) 'Localized EMT reprograms glial progenitors to promote
1133 spinal cord repair', *Developmental cell* 56(5): 613-626 e7.

1134 Kole, C., Brommer, B., Nakaya, N., Sengupta, M., Bonet-Ponce, L., Zhao, T., Wang, C., Li, W.,
1135 He, Z. and Tomarev, S. (2020) 'Activating Transcription Factor 3 (ATF3) Protects Retinal Ganglion
1136 Cells and Promotes Functional Preservation After Optic Nerve Crush', *Invest Ophthalmol Vis Sci*
1137 61(2): 31.

1138 Kuscha, V., Frazer, S. L., Dias, T. B., Hibi, M., Becker, T. and Becker, C. G. (2012) 'Lesion-
1139 induced generation of interneuron cell types in specific dorsoventral domains in the spinal cord of
1140 adult zebrafish', *J Comp Neurol* 520(16): 3604-16.

1141 Lacar, B., Linker, S. B., Jaeger, B. N., Krishnaswami, S. R., Barron, J. J., Kelder, M. J. E., Parylak,
1142 S. L., Paquola, A. C. M., Venepally, P., Novotny, M. et al. (2016) 'Nuclear RNA-seq of single
1143 neurons reveals molecular signatures of activation', *Nat Commun* 7: 11022.

1144 Lake, B. B., Codeluppi, S., Yung, Y. C., Gao, D., Chun, J., Kharchenko, P. V., Linnarsson, S. and
1145 Zhang, K. (2017) 'A comparative strategy for single-nucleus and single-cell transcriptomes
1146 confirms accuracy in predicted cell-type expression from nuclear RNA', *Sci Rep* 7(1): 6031.

1147 Lange, M., Bergen, V., Klein, M., Setty, M., Reuter, B., Bakhti, M., Lickert, H., Ansari, M.,
1148 Schniering, J., Schiller, H. B. et al. (2022) 'CellRank for directed single-cell fate mapping', *Nat*
1149 *Methods* 19(2): 159-170.

1150 Lawson, N. D., Li, R., Shin, M., Grosse, A., Yukselen, O., Stone, O. A., Kucukural, A. and Zhu, L.
1151 (2020) 'An improved zebrafish transcriptome annotation for sensitive and comprehensive
1152 detection of cell type-specific genes', *Elife* 9.

1153 Levine, J. H., Simonds, E. F., Bendall, S. C., Davis, K. L., Amir el, A. D., Tadmor, M. D., Litvin,
1154 O., Fienberg, H. G., Jager, A., Zunder, E. R. et al. (2015) 'Data-Driven Phenotypic Dissection of
1155 AML Reveals Progenitor-like Cells that Correlate with Prognosis', *Cell* 162(1): 184-97.

1156 Li, W. R., Wang, Y. L., Li, C., Gao, P., Zhang, F. F., Hu, M., Li, J. C., Zhang, S., Li, R. and Zhang,
1157 C. X. (2021) 'Synaptotagmin-11 inhibits spontaneous neurotransmission through vti1a', *J*
1158 *Neurochem* 159(4): 729-741.

1159 Lin, P. Y., Chanaday, N. L., Horvath, P. M., Ramirez, D. M. O., Monteggia, L. M. and Kavalali, E.
1160 T. (2020) 'VAMP4 Maintains a Ca(2+)-Sensitive Pool of Spontaneously Recycling Synaptic
1161 Vesicles', *J Neurosci* 40(28): 5389-5401.

1162 Lu, D. C., Niu, T. and Alaynick, W. A. (2015) 'Molecular and cellular development of spinal cord
1163 locomotor circuitry', *Front Mol Neurosci* 8: 25.

1164 Matson, K. J. E., Russ, D. E., Kathe, C., Hua, I., Maric, D., Ding, Y., Krynitsky, J., Pursley, R.,
1165 Sathyamurthy, A., Squair, J. W. et al. (2022) 'Single cell atlas of spinal cord injury in mice reveals
1166 a pro-regenerative signature in spinocerebellar neurons', *Nat Commun* 13(1): 5628.

1167 Matson, K. J. E., Sathyamurthy, A., Johnson, K. R., Kelly, M. C., Kelley, M. W. and Levine, A. J.
1168 (2018) 'Isolation of Adult Spinal Cord Nuclei for Massively Parallel Single-nucleus RNA
1169 Sequencing', *Journal of visualized experiments : JoVE*(140).

1170 Mikami, T., Yasunaga, D. and Kitagawa, H. (2009) 'Contactin-1 is a functional receptor for
1171 neuroregulatory chondroitin sulfate-E', *J Biol Chem* 284(7): 4494-9.

1172 Milich, L. M., Choi, J. S., Ryan, C., Cerqueira, S. R., Benavides, S., Yahn, S. L., Tsoulfas, P. and
1173 Lee, J. K. (2021) 'Single-cell analysis of the cellular heterogeneity and interactions in the injured
1174 mouse spinal cord', *J Exp Med* 218(8).

1175 Milich, L. M., Ryan, C. B. and Lee, J. K. (2019) 'The origin, fate, and contribution of macrophages
1176 to spinal cord injury pathology', *Acta Neuropathol* 137(5): 785-797.

1177 Mokalled, M. H., Patra, C., Dickson, A. L., Endo, T., Stainier, D. Y. and Poss, K. D. (2016) 'Injury-
1178 induced ctgfa directs glial bridging and spinal cord regeneration in zebrafish', *Science* 354(6312):
1179 630-634.

1180 Nakamura, Y., Ueno, M., Niehaus, J. K., Lang, R. A., Zheng, Y. and Yoshida, Y. (2021)
1181 'Modulation of Both Intrinsic and Extrinsic Factors Additively Promotes Rewiring of Corticospinal
1182 Circuits after Spinal Cord Injury', *J Neurosci* 41(50): 10247-10260.

1183 Nicholson-Fish, J. C., Kokotos, A. C., Gillingwater, T. H., Smillie, K. J. and Cousin, M. A. (2015)
1184 'VAMP4 Is an Essential Cargo Molecule for Activity-Dependent Bulk Endocytosis', *Neuron* 88(5):
1185 973-984.

1186 Park, K. K., Liu, K., Hu, Y., Smith, P. D., Wang, C., Cai, B., Xu, B., Connolly, L., Kramvis, I., Sahin,
1187 M. et al. (2008) 'Promoting axon regeneration in the adult CNS by modulation of the PTEN/mTOR
1188 pathway', *Science* 322(5903): 963-6.

1189 R Core Team (2018) R: A language and environment for statistical computing, https://www.R-
1190 project.org/.

1191 Reimer, M. M., Kuscha, V., Wyatt, C., Sorensen, I., Frank, R. E., Knuwer, M., Becker, T. and
1192 Becker, C. G. (2009) 'Sonic hedgehog is a polarized signal for motor neuron regeneration in adult
1193 zebrafish', *J Neurosci* 29(48): 15073-82.

1194 Reimer, M. M., Sorensen, I., Kuscha, V., Frank, R. E., Liu, C., Becker, C. G. and Becker, T. (2008)
1195 'Motor neuron regeneration in adult zebrafish', *The Journal of neuroscience : the official journal*
1196 *of the Society for Neuroscience* 28(34): 8510-6.

1197 Ren, Y., Ao, Y., O'Shea, T. M., Burda, J. E., Bernstein, A. M., Brumm, A. J., Muthusamy, N.,
1198 Ghashghaei, H. T., Carmichael, S. T., Cheng, L. et al. (2017) 'Ependymal cell contribution to scar
1199 formation after spinal cord injury is minimal, local and dependent on direct ependymal injury', *Sci*
1200 *Rep* 7: 41122.

1201 Rodrigo Albors, A., Singer, G. A., Llorens-Bobadilla, E., Frisen, J., May, A. P., Ponting, C. P. and
1202 Storey, K. G. (2023) 'An ependymal cell census identifies heterogeneous and ongoing cell
1203 maturation in the adult mouse spinal cord that changes dynamically on injury', *Developmental cell*
1204 58(3): 239-255 e10.

1205 Rosenberg, A. B., Roco, C. M., Muscat, R. A., Kuchina, A., Sample, P., Yao, Z., Graybuck, L. T.,
1206 Peeler, D. J., Mukherjee, S., Chen, W. et al. (2018) 'Single-cell profiling of the developing mouse
1207 brain and spinal cord with split-pool barcoding', *Science* 360(6385): 176-182.

1208 Rossum, G.V. and Drake, F.L. (2009) Python 3 Reference Manual.

1209 Rougeot, J., Torraca, V., Zakrzewska, A., Kanwal, Z., Jansen, H. J., Sommer, F., Spaink, H. P.
1210 and Meijer, A. H. (2019) 'RNAseq Profiling of Leukocyte Populations in Zebrafish Larvae Reveals
1211 a cxcl11 Chemokine Gene as a Marker of Macrophage Polarization During Mycobacterial
1212 Infection', *Front Immunol* 10: 832.

1213 Salic, A. and Mitchison, T. J. (2008) 'A chemical method for fast and sensitive detection of DNA
1214 synthesis in vivo', *Proc Natl Acad Sci U S A* 105(7): 2415-20.

1215 Saraswathy, V. M., Zhou, L., McAdow, A. R., Burris, B., Dogra, D., Reischauer, S. and Mokalled,
1216 M. H. (2022) 'Myostatin is a negative regulator of adult neurogenesis after spinal cord injury in
1217 zebrafish', *Cell Rep* 41(8): 111705.

1218 Sathyamurthy, A., Johnson, K. R., Matson, K. J. E., Dobrott, C. I., Li, L., Ryba, A. R., Bergman,
1219 T. B., Kelly, M. C., Kelley, M. W. and Levine, A. J. (2018) 'Massively Parallel Single Nucleus
1220 Transcriptional Profiling Defines Spinal Cord Neurons and Their Activity during Behavior', *Cell*
1221 *Rep* 22(8): 2216-2225.

1222 Satou, C., Kimura, Y., Hirata, H., Suster, M. L., Kawakami, K. and Higashijima, S. (2013)
1223 'Transgenic tools to characterize neuronal properties of discrete populations of zebrafish
1224 neurons', *Development* 140(18): 3927-31.

1225 Scott, K., O'Rourke, R., Winkler, C. C., Kearns, C. A. and Appel, B. (2021) 'Temporal single-cell
1226 transcriptomes of zebrafish spinal cord pMN progenitors reveal distinct neuronal and glial
1227 progenitor populations', *Dev Biol* 479: 37-50.

1228 Shah, P. T., Stratton, J. A., Stykel, M. G., Abbasi, S., Sharma, S., Mayr, K. A., Koblinger, K.,
1229 Whelan, P. J. and Biernaskie, J. (2018) 'Single-Cell Transcriptomics and Fate Mapping of
1230 Ependymal Cells Reveals an Absence of Neural Stem Cell Function', *Cell* 173(4): 1045-1057 e9.

1231 Shimojo, M., Madara, J., Pankow, S., Liu, X., Yates, J., 3rd, Sudhof, T. C. and Maximov, A. (2019)
1232 'Synaptotagmin-11 mediates a vesicle trafficking pathway that is essential for development and
1233 synaptic plasticity', *Genes Dev* 33(5-6): 365-376.

1234 Sofroniew, M. V. (2018) 'Dissecting spinal cord regeneration', *Nature* 557(7705): 343-350.

1235 Stassen, S. V., Yip, G. G. K., Wong, K. K. Y., Ho, J. W. K. and Tsia, K. K. (2021) 'Generalized
1236 and scalable trajectory inference in single-cell omics data with VIA', *Nat Commun* 12(1): 5528.

1237 Stuart, T., Butler, A., Hoffman, P., Hafemeister, C., Papalexi, E., Mauck, W. M., 3rd, Hao, Y.,
1238 Stoeckius, M., Smibert, P. and Satija, R. (2019) 'Comprehensive Integration of Single-Cell Data',
1239 *Cell* 177(7): 1888-1902 e21.

1240 Tambalo, M., Mitter, R. and Wilkinson, D. G. (2020) 'A single cell transcriptome atlas of the
1241 developing zebrafish hindbrain', *Development* 147(6).

1242 Tang, Q., Iyer, S., Lobbardi, R., Moore, J. C., Chen, H., Lareau, C., Hebert, C., Shaw, M. L.,
1243 Neftel, C., Suva, M. L. et al. (2017) 'Dissecting hematopoietic and renal cell heterogeneity in adult
1244 zebrafish at single-cell resolution using RNA sequencing', *J Exp Med* 214(10): 2875-2887.

1245 Tran, A. P., Warren, P. M. and Silver, J. (2022) 'New insights into glial scar formation after spinal
1246 cord injury', *Cell Tissue Res* 387(3): 319-336.

1247 van den Brink, S. C., Sage, F., Vertesy, A., Spanjaard, B., Peterson-Maduro, J., Baron, C. S.,
1248 Robin, C. and van Oudenaarden, A. (2017) 'Single-cell sequencing reveals dissociation-induced
1249 gene expression in tissue subpopulations', *Nat Methods* 14(10): 935-936.

1250 Vandestadt, C., Vanwalleghem, G. C., Khabooshan, M. A., Douek, A. M., Castillo, H. A., Li, M.,
1251 Schulze, K., Don, E., Stamatis, S. A., Ratnadiwakara, M. et al. (2021) 'RNA-induced inflammation
1252 and migration of precursor neurons initiates neuronal circuit regeneration in zebrafish',
1253 *Developmental cell* 56(16): 2364-2380 e8.

1254 Walsh, F. S. and Doherty, P. (1996) 'Cell adhesion molecules and neuronal regeneration', *Curr*
1255 *Opin Cell Biol* 8(5): 707-13.

1256 Wang, C., Wang, Y., Hu, M., Chai, Z., Wu, Q., Huang, R., Han, W., Zhang, C. X. and Zhou, Z.
1257 (2016) 'Synaptotagmin-11 inhibits clathrin-mediated and bulk endocytosis', *EMBO Rep* 17(1): 47-
1258 63.

1259 Wang, L. F., Huang, S. B., Zhao, H. D., Liu, C. J., Yao, L. and Shen, Y. Q. (2017) 'Activating
1260 transcription factor 3 promotes spinal cord regeneration of adult zebrafish', *Biochem Biophys Res*
1261 *Commun* 488(3): 522-527.

1262 Wang, Z., Reynolds, A., Kirry, A., Nienhaus, C. and Blackmore, M. G. (2015) 'Overexpression of
1263 Sox11 promotes corticospinal tract regeneration after spinal injury while interfering with functional
1264 recovery', *J Neurosci* 35(7): 3139-45.

1265 Wu, H., Kirita, Y., Donnelly, E. L. and Humphreys, B. D. (2019) 'Advantages of Single-Nucleus
1266 over Single-Cell RNA Sequencing of Adult Kidney: Rare Cell Types and Novel Cell States
1267 Revealed in Fibrosis', *J Am Soc Nephrol* 30(1): 23-32.

1268 Xu, C. and Su, Z. (2015) 'Identification of cell types from single-cell transcriptomes using a novel
1269 clustering method', *Bioinformatics* 31(12): 1974-80.

1270 Yadav, A., Matson, K. J. E., Li, L., Hua, I., Petrescu, J., Kang, K., Alkaslasi, M. R., Lee, D. I.,
1271 Hasan, S., Galuta, A. et al. (2023) 'A cellular taxonomy of the adult human spinal cord', *Neuron*
1272 111(3): 328-344 e7.

1273 Yao, C., Cao, Y., Wang, D., Lv, Y., Liu, Y., Gu, X., Wang, Y., Wang, X. and Yu, B. (2022) 'Single-
1274 cell sequencing reveals microglia induced angiogenesis by specific subsets of endothelial cells
1275 following spinal cord injury', *FASEB J* 36(7): e22393.

1276 Zappia, L. and Oshlack, A. (2018) 'Clustering trees: a visualization for evaluating clusterings at
1277 multiple resolutions', *Gigascience* 7(7).

1278 Zeisel, A., Hochgerner, H., Lonnerberg, P., Johnsson, A., Memic, F., van der Zwan, J., Haring,
1279 M., Braun, E., Borm, L. E., La Manno, G. et al. (2018) 'Molecular Architecture of the Mouse
1280 Nervous System', *Cell* 174(4): 999-1014 e22.

1281 Zhang, H., Fang, X., Huang, D., Luo, Q., Zheng, M., Wang, K., Cao, L. and Yin, Z. (2018)
1282 'Erythropoietin signaling increases neurogenesis and oligodendrogenesis of endogenous neural
1283 stem cells following spinal cord injury both in vivo and in vitro', *Mol Med Rep* 17(1): 264-272.

1284 Zhang, Y., Chen, K., Sloan, S. A., Bennett, M. L., Scholze, A. R., O'Keeffe, S., Phatnani, H. P.,
1285 Guarnieri, P., Caneda, C., Ruderisch, N. et al. (2014) 'An RNA-sequencing transcriptome and
1286 splicing database of glia, neurons, and vascular cells of the cerebral cortex', *J Neurosci* 34(36):
1287 11929-47.

1288 Zhang, Y., Yeh, J., Richardson, P. M. and Bo, X. (2008) 'Cell adhesion molecules of the
1289 immunoglobulin superfamily in axonal regeneration and neural repair', *Restor Neurol Neurosci*
1290 26(2-3): 81-96.

1291 Zhou, Y., Zhou, B., Pache, L., Chang, M., Khodabakhshi, A. H., Tanaseichuk, O., Benner, C. and
1292 Chanda, S. K. (2019) 'Metascape provides a biologist-oriented resource for the analysis of
1293 systems-level datasets', *Nat Commun* 10(1): 1523.

Zhu, Y., Soderblom, C., Trojanowsky, M., Lee, D. H. and Lee, J. K. (2015) 'Fibronectin Matrix Assembly after Spinal Cord Injury', *J Neurotrauma* 32(15): 1158-67.